On Dynamics of Rigid Sphere-reinforced Metacomposite Beams and Rods

by

Jiacen Meng

A thesis submitted in partial fulfillment of the requirements for the degree of

Master of Science

Department of Mechanical Engineering
University of Alberta

Abstract

An analytical model is presented to study dynamic behaviors of rigid sphere-reinforced random metacomposites. The model is based on the concept that the deviation of the displacement field of embedded rigid spheres from the displacement field of the composite is responsible for novel dynamic behaviors of stiff sphere-reinforced metacomposites. Compared to the existing models, the present model offers a simple general method to analyze dynamic problems of rigid sphere-reinforced random metacomposites, and its validity and efficiency are demonstrated by comparing the predicted results for bandgap with known experimental or numerical data on several typical steel/glass/lead-polymer metacomposites. Several basic dynamic problems of rigid sphere-reinforced metacomposite beams and rods are investigated, and some novel dynamic phenomena (such as vibration isolation, localized buckling, and natural frequency within the bandgap caused by an attached concentrated mass) are demonstrated. The main results include: 1). natural frequencies of a rigid sphere-reinforced metacomposite beam or rod always stay outside of the bandgap, independent of all other material and geometrical parameters, while a concentrated mass attached to the free end of a rod may cause a natural frequency within the bandgap. 2). a rigid sphere-reinforced metacomposite beam or rod can exhibit vibration isolation phenomena so that the forced vibration is highly localized near the site of the applied external periodic excitation and vanishing small in all other parts of the beam or rod when the external excitation frequency falls within the bandgap, while the forced vibration does spread into the entire beam or rod when the excitation frequency is out of the bandgap. 3). a hinged rigid sphere-reinforced metacomposite beam under a constant compressive load can exhibit localized buckling at the critical buckling state when the mass ratio of the rigid-sphere phase to the matrix phase is vanishingly small.

Preface

Chapters 2, 3, 4.1, 4.2, 5.2 and 5.3 of the thesis are largely taken from a published journal article by J.C. Meng & C.Q. Ru, “Effective mass density of rigid sphere-reinforced elastic composites,” Meccanica, 56, pp.1209–1221 (2021). For this published journal article, I was responsible for math derivation, obtaining results. Dr. Ru, C.Q. was the supervisory author who proposed the topic, checked the results and revised the manuscript.

Acknowledgment

I would like to thank my supervisor Dr. C.Q. Ru for his encouragement and support during my study. I sincerely appreciate his patience for me especially when my personal health was not in a good condition. I also thank all fellow researchers in Department of Mechanical Engineering at the University of Alberta and my family and friends who have helped and supported me all the time. Finally, I want to thank the financial support from NSERC during my study.

Table of Contents

Abstract ii

Preface iii

Acknowledgment iv

List of Figures vii

List of Tables ix

Chapter 1 Introduction 1

1.1 Literature review 1

1.1.1 Locally resonant metamaterials 1

1.1.2 Existing models for particle-reinforced metamaterials 2

1.2 Objectives of this research 4

Chapter 2 Dynamic equations for rigid sphere-reinforced random metacomposites 6

2.1 Relation between $u_{\mathrm{mass}}(x,t)$ and $u(x,t)$ 7

2.2 An expression for the spring constant β 9

Chapter 3 Effective mass density and the bandgap 11

3.1 Effective mass density and the bandgap 11

3.2 Comparison to known data 13

Chapter 4 Vibration and buckling of a rigid sphere-reinforced metacomposite beam 17

4.1 Free vibration of a hinged or cantilever beam 17

4.2 Dynamic buckling of a hinged beam 21

4.3 Forced vibration driven by vibrating ends 23

4.3.1 A hinged beam with two vibrating ends 23

4.3.2 Vibration isolation of a hinged beam 25

4.3.3 A cantilever beam with a vibrating built-in end 27

4.3.4 Vibration isolation of a cantilever beam 30

4.4 Forced vibration of a hinged beam driven by an external harmonic force 32

4.4.1 Forced vibration driven by a point force at midway 32

4.4.2 Vibration isolation under a point force at midway 33

Chapter 5 Vibration of a rigid sphere-reinforced metacomposite rod 38

5.1 Free vibration of a metacomposite rod 38

5.2 Vibration isolation of a metacomposite rod 40

5.3 Free vibration of a metacomposite rod with an attached mass at its end 43

Chapter 6 Conclusions and future work 47

6.1 Conclusions 47

6.2 Future work 48

Bibliography 49

List of Figures

Fig. 2.1 Rigid sphere-spring composite model (where ρ_m is the mass density of the matrix phase, ρ_s is the mass density of the rigid spheres, $\boldsymbol{u}$ is the displacement field of the composite, $\boldsymbol{u}_s$ is the displacement field of the embedded rigid spheres and β is the spring constant per unit volume of the composite)

Fig. 4.1 Natural frequencies (f=$\omega/2\pi$) of a hinged steel sphere-polyester composite beam, as a function of the mode number m for different volume fractions, of a circular cross-section with the diameter D=1cm, the length L=10D, and the radius of steel spheres R=0.5 mm, where ρ_s= 7800 kg/m^3, ρ_m= 1220 kg/m^3, $(c_s)_m$=1180 m/s and $(c_l)_m$=2490 m/s

Fig. 4.2 Natural frequencies of a steel sphere-polyester composite cantilever beam, as a function of λ for different volume fractions, of a circular cross-section with the diameter D=1cm, the length L=10D, and the radius of steel spheres R=0.5 mm, where ρ_s= 7800 kg/m^3, ρ_m= 1220 kg/m^3, $(c_s)_m$=1180 m/s and $(c_l)_m$=2490 m/s

Fig. 4.3 A schematic diagram of a hinged beam driven by two vibrating ends

Fig. 4.4 Forced vibration mode of a hinged steel sphere-polyester composite beam driven by two vibrating ends under different excitation frequencies ω: (a) $\omega < \omega_0$, (b) $\omega_0 < \omega < \omega_u$ and (c) $\omega > \omega_u$, where D=1cm, L=10D, R=0.5 mm, ρ_s= 7800 kg/m^3, ρ_m= 1220 kg/m^3, $(c_s)_m$=1180 m/s, $(c_l)_m$=2490 m/s and δ=0.184

Fig. 4.5 Forced vibrational mode of a hinged steel sphere-polyester composite beam driven by two vibrating ends with different length-to-diameter ratio, where ω=0.90ω_u, D=1cm, R=0.5 mm, ρ_s= 7800 kg/m^3, ρ_m= 1220 kg/m^3, $(c_s)_m$=1180 m/s, $(c_l)_m$=2490 m/s and δ=0.184

Fig. 4.6 A schematic diagram of a cantilever beam driven by a vibrating built-in end

Fig. 4.7 Transmission coefficient of the metamaterial cantilever beam [46] consisting of lead spheres, silicon rubber coating and epoxy matrix under different excitation frequencies, where L=1 m, A=300 mm^2, I=22500 mm^4, R=3 mm, ρ_s= 11600 kg/m^3, ρ_m= 1180 kg/m^3, E_m=4.252×10^9 Pa and δ=0.113

Fig. 4.8 Forced vibration mode of a steel sphere-polyester composite cantilever beam driven by a vibrating built-in end under different excitation frequencies ω: (a) $\omega < \omega_0$, (b) $\omega_0 < \omega < \omega_u$ and (c) $\omega > \omega_u$, where D=1cm, L=10D, R=0.5 mm, ρ_s= 7800 kg/m^3, ρ_m= 1220 kg/m^3, $(c_s)_m$=1180 m/s, $(c_l)_m$=2490 m/s and δ=0.184

Fig. 4.9 Forced vibrational mode of a steel sphere-polyester composite cantilever beam driven by a vibrating built-in end with different length-to-diameter ratio, where ω=0.90ω_u, D=1cm, R=0.5 mm, ρ_s= 7800 kg/m^3, ρ_m= 1220 kg/m^3, $(c_s)_m$=1180 m/s, $(c_l)_m$=2490 m/s and δ=0.184

Fig. 4.10 A schematic diagram of a hinged beam driven by a point force at midway

Fig. 4.11 Forced vibration mode of a hinged steel sphere-polyester composite beam driven by a point force at its midway under different excitation frequencies ω: (a) $\omega < \omega_0$, (b) $\omega_0 < \omega < \omega_u$ and (c) $\omega > \omega_u$, where D=1 cm, L=10D, R=0.5 mm, ρ_s= 7800 kg/m^3, ρ_m= 1220 kg/m^3, $(c_s)_m$=1180 m/s, $(c_l)_m$=2490 m/s, δ=0.184 and Q_0=80 kN

Fig 4.12 Maximum deflection of a hinged steel sphere-polyester composite beam driven by a point force at its midway under different excitation frequencies within the bandgap, where D=1 cm, L=10D, R=0.5 mm, ρ_s= 7800 kg/m^3, ρ_m= 1220 kg/m^3, $(c_s)_m$=1180 m/s, $(c_l)_m$=2490 m/s, δ=0.184 and Q_0=80 kN

Fig. 4.13 Amplitude of the forced vibration of a hinged steel sphere-polyester composite beam at (a) x/L=0.5 & (b) x/L=0.8 under different values of the midpoint force Q_0, where D=1 cm, L=10D, R=0.5 mm, ρ_s= 7800 kg/m^3, ρ_m= 1220 kg/m^3, $(c_s)_m$=1180 m/s, $(c_l)_m$=2490 m/s and δ=0.184

Fig. 4.14 Forced vibrational mode of a hinged steel sphere-polyester composite beam driven by a point force at its midway with different length-to-diameter ratio, where ω=0.90ω_u, D=1 cm, R=0.5 mm, ρ_s= 7800 kg/m^3, ρ_m= 1220 kg/m^3, $(c_s)_m$=1180 m/s, $(c_l)_m$=2490 m/s, δ=0.184 and Q_0=80 kN

Fig. 4.15 Forced vibrational mode of a hinged steel sphere-polyester composite beam under different values of the midpoint force Q_0, where ω=0.90ω_u, D=1 cm, L=10D, R=0.5 mm, ρ_s= 7800 kg/m^3, ρ_m= 1220 kg/m^3, $(c_s)_m$=1180 m/s, $(c_l)_m$=2490 m/s and δ=0.184

Fig. 5.1 Natural frequencies of a steel sphere-polyester composite rod, as a function of the mode number m for different volume fractions, with the length L=5 cm and the radius of steel spheres R=0.5 mm, where ρ_s= 7800 kg/m^3, ρ_m= 1220 kg/m^3, $(c_s)_m$=1180 m/s and $(c_l)_m$=2490 m/s

Fig. 5.2 A schematic diagram of a rod with a fixed end and driven by a harmonic axial displacement at its free end

Fig. 5.3 Forced vibrational mode of a steel sphere-reinforced polyester rod driven by a harmonic axial displacement at the free end x=L (L=5 cm) under different excitation frequencies ω: (a) $\omega < \omega_0$, (b) $\omega_0 < \omega < \omega_u$ and (c) $\omega > \omega_u$, where ρ_s= 7800 kg/m^3, ρ_m= 1220 kg/m^3, $(c_s)_m$=1180 m/s, $(c_l)_m$=2490 m/s, R=0.5 mm and δ=0.184

Fig. 5.4 Forced vibrational mode of a steel sphere-reinforced polyester rod driven by a harmonic axial displacement at the free end x=L with different length (L), where ω=0.90ω_u, R=0.5 mm, ρ_s= 7800 kg/m^3, ρ_m= 1220 kg/m^3, $(c_s)_m$=1180 m/s, $(c_l)_m$=2490 m/s and δ=0.184

Fig. 5.5 A schematic diagram of a rod with a fixed end and an attached mass at its free end

Fig. 5.6 Plots of the function $f(\lambda)$ defined by eq.(5.18) at different values of m_0 and χ/m_0 with the parameters of steel sphere-reinforced polyester, ρ_s= 7800 kg/m^3, ρ_m= 1220 kg/m^3 and δ=0.184

Fig. 5.7 The α-ω_2 (or ω_1) relation for free vibration of a steel sphere-reinforced polyester rod fixed at the end x=0 and with a mass attached to the other end x=L, where ρ_s= 7800 kg/m^3, ρ_m= 1220 kg/m^3, R=0.5 mm, L=5 cm and m_0=1

List of Tables

Table 3.1 Comparison between the present results and the experimental data for a glass sphere polyester composite

Chapter 1

Introduction

1.1 Literature review

Elastic metamaterials are a new kind of elastic composites which exhibit exceptional dynamic properties not discovered in nature or traditional materials. Metamaterials were initially introduced for electromagnetic wave [1]. Veselago [1] theoretically proposed the materials with negative characteristic parameters that affected the electromagnetic wave propagation. Later, the investigation of metamaterials has been extended to the field of mechanical and acoustic waves. Many researches on vibrational wave propagation and dynamic behaviors in metamaterials emerged over the past years [2-22]. It was found that the man-made artificial microstructure of metamaterials can truly make a difference to the vibrational modes at some frequencies that constitute a spectral range of frequencies called “bandgap” within which vibration and wave propagation are largely attenuated or forbidden.

1.1.1 Locally resonant metamaterials

One of the important causes of bandgap is “locally resonant” microstructure that can make “negative effective mass (density)”, which gives birth to a type of metamaterials called “locally resonant metamaterials”. However, negative effective mass (density) is not an actually existing property in real materials, but a concept introduced for determining the frequency range of bandgap. The common interpretation for the formation of negative effective mass is put forward through a simple mass-in-mass structure with a spring connecting the masses [2-4]. Effective mass becomes negative because the internal spring force between the masses is larger than the external force applied to the mass-in-mass system (see e.g., fig.2(a) in [2] or [3]).

The locally resonant metamaterials have stimulated many researchers’ interests in recent years [2-11] due to its interesting vibration attenuation performance with the negative effective mass (density). Firstly, Liu et al. [5] proposed a type of phononic crystals constructed of lead balls coated with silicone rubber (acting as a spring) in an epoxy matrix. The relevant bandgap phenomena due to the locally resonant microstructure were captured by observing the sound transmission in phononic crystals. Moreover, it was indicated that the local resonance bandgap can suppress the vibration at wavelengths two orders larger than the interparticle distance (called "lattice constant"). So, the local resonance bandgap is usually applied to the low-frequency vibration attenuation/ isolation. Further, Sigalas et al. [6] wrote a review about the estimation of bandgaps from vibrational modes of various phononic crystals. In his section 15.5 [6], he also mentioned that the local resonance can be generated in phononic crystals by coating the scatterers with some elastic soft materials. Also, Calius et al. [7] showed some experimental and numerical results of the frequency response and transmission loss for the similar microstructures which exhibited significant local resonance bandgap behaviors.

In addition to phononic crystals, some locally resonant metamaterial models were developed for the broadband vibration suppression/ isolation owing to the narrow width of the local resonance bandgap [8, 9]. For example, the uniform beam with numerous spring-mass-damper subsystems was devised by Sun et al. [2] based on the idea of the locally resonant microstructure. The spring-mass-damper subsystems acting as local resonators achieved the vibration isolation through generating the negative effective mass. Further, Pai et al. [3] added one more mass to the original spring-mass-damper subsystems in [2] to improve the vibration attenuation performance via creating two bandgaps. Apart from the vibration isolation within either of bandgaps, the vibration can be suppressed when the excitation frequency was out of but between the two bandgaps. Besides, a chiral metamaterial beam [10] was proposed for the broadband low-frequency vibration suppression, where local resonators consisted of metal cylinders coated with rubber and embedded in the hexagonal chiral lattice. Moreover, Schiavone & Wang [11] developed a new continuous model for a sort of metamaterials characterized by local rotations coupling with macro-translations from a rigid disk-spring discrete system. And a wider bandgap may be achieved through their continuum model with double negative properties [11].

1.1.2 Existing models for particle-reinforced metamaterials

An important class of metamaterials is stiff sphere-reinforced metacomposites [12-28] in which the elastic modulus of the embedded spheres is much higher than that of the compliant elastic matrix, such as steel or glass sphere-reinforced polymer composites. There are some early models established for studying dynamic behaviors of this type of metacomposites. Moon and Mow [12] initially attempted to derive a one-dimensional dynamic model for the wave propagation in a rigid sphere-reinforced random metacomposite with a small volume fraction of spheres. However, finally, their derivation stopped at the governing equations of motion for both sphere and matrix through the Lagrange's equation combined with Lagrangian and dissipation functions. Later, their model was validated by Kinra and Li [14] via comparing to the experimentally measured resonance frequency for a lead/epoxy composite. Some new micromechanical models [15] were developed for mechanical behaviors of particle-reinforced composites based on a modified Mori-Tanaka method with considering the mutual interaction of particles. Besides, Kinra et al. [17] experimentally measured the transmission of a plane longitudinal wave through a layer of lead spheres in a polyester matrix. Then, Maslov and Kinra [18] measured the same wave through a periodic layer of rigid spheres at wavelengths comparable to the characteristic length of the composite. Finally, an approximate low-frequency model was developed and validated for a plane longitudinal wave normally incident on a periodic layer of rigid spheres in an elastic matrix with the multiple-scattering effect. Furthermore, Cheng et al. [21] put forward a method via incorporating experiments, numerical simulations and theoretical analysis to study the high-frequency attenuation mechanism of polyurea-matrix particulate composites. And Rahimzadeh [22] applied the Sabina-Willis model to analyzing effective dynamic properties for the propagation of P and S waves in particulate composites.

Additionally, some models were employed for the evaluation of elastic properties of particle-reinforced metamaterials, for instance, 3D representative volume element (RVE) model [23, 24]. Segurado & Llorca [23] and Kari et al. [24] calculated elastic constants with RVE respectively by the common finite element method (FEM) and a numerical homogenization technique based on FEM. Other than RVE, a theoretical cube-within-cube formation [25], isotropized Voigt-Reuss model [26] and microstructure-free finite element modeling (MF-FEM) [27] were also the existing tools to estimate the elastic moduli. The Voigt-Reuss model [26] is applicable to the composite with either large or small contrast of phase properties while MF-FEM [27] had a good performance only with small contrast of phase properties. Besides, the axial stiffness of the springs connecting cells was computed by a lattice model [28] especially in the composites with a large volume fraction of particles.

1.2 Objectives of this research

In most cases, complicated numerical calculations and experiments are required to analyze dynamics of such stiff sphere-reinforced metacomposites. And also, the majority of existing researches have been limited to periodic composites [12-28]. Indeed, it is of great interest to develop simpler analytical models for dynamics of stiff sphere-reinforced random metacomposites. The present work aims to propose a new and simple, though approximate, analytical model to analyze dynamic behaviors of stiff sphere-reinforced random metacomposites. The proposed model is based on the concept that the deviation of the displacement field of embedded stiff spheres from the displacement field of the composite is responsible for novel dynamic behaviors of the composites. Unlike some existing models [12-28] which were based on rather complex mathematical formulation and numerical calculation, our model is mathematically simple. Actually, as shown in this thesis, the present model gives classical elastodynamic equations combined with a simple differential relation between the displacement field of the mass centre of representative unit cell and the displacement field of composite. Our model ignores the complicated microstructure of the composite and treats the composite as a homogeneous isotropic effective elastic body defined by the two effective elastic constants. Therefore, the proposed model should be limited to the cases when the characteristic wavelength of the displacement field is larger than the diameter of embedded rigid spheres. Besides, it could offer a general simple model to study dynamics of stiff sphere-reinforced metacomposites.

Specifically, the thesis includes:

(1) In Chapter 2, the governing equations of the proposed model are derived for dynamics of rigid sphere-reinforced random metacomposites.

(2) In Chapter 3, the effective mass density and the bandgap are determined based on the equations derived in Chapter 2 for a rigid sphere-reinforced metacomposite, and the proposed model is validated by comparing its predicted bandgap frequencies to known experimental and numerical data.

(3) In Chapters 4 and 5, the proposed model is used to study several basic dynamic problems of rigid sphere-reinforced metacomposite beams and rods, respectively. In Chapter 4, firstly, the free vibration and corresponding natural frequencies are studied for a rigid

sphere-reinforced metacomposite hinged or cantilever beam, and dynamic buckling is discussed for the hinged beam. Next, the equations of motion are derived for the forced vibrations of both hinged and cantilever beams driven by vibrating ends and the hinged beam under an external force, and the relevant vibration isolation phenomena are discussed. In Chapter 5, the free vibration and vibration isolation under a periodic axial displacement are demonstrated for a rigid sphere-reinforced metacomposite rod, and the free vibration of a rod with an attached mass at its free end is analyzed as well.

(4) In Chapter 6, major conclusions are summarized and future work is recommended.

Chapter 2

Dynamic equations for rigid sphere-reinforced random metacomposites

In this chapter, we will develop a rigid sphere-spring composite model with one of important assumptions—— “rigid spheres” which means the elastic moduli of embedded spheres are much larger than that of the soft matrix phase.

First of all, let us consider an isotropic rigid sphere-reinforced metacomposite comprised of a compliant isotropic elastic matrix phase, of Young’s modulus E_m and Poisson ratio ν_m, and reinforced by randomly distributed rigid spheres of radius R. It is now widely recognized [12-20] that the deviation of the displacement field of embedded stiff spheres from the displacement field of the composite is responsible for novel dynamic behaviors of stiff sphere-reinforced metacomposites. Thus, let us consider two displacement fields: the displacement field $\boldsymbol{u}(\boldsymbol{x},t)$ of the composite and the displacement field $\boldsymbol{u}_{\mathrm{s}}(\boldsymbol{x},t)$ of the embedded rigid spheres.

And the equations of motion of the metacomposite in the absence of body forces are of the form

$$\rho\frac{\partial^2 u_{mass}}{\partial t^2}=\frac{\partial\sigma_{11}}{\partial x}+\frac{\partial\sigma_{12}}{\partial y}+\frac{\partial\sigma_{13}}{\partial z},$$

$$\rho\frac{\partial^2 v_{mass}}{\partial t^2}=\frac{\partial\sigma_{12}}{\partial x}+\frac{\partial\sigma_{22}}{\partial y}+\frac{\partial\sigma_{23}}{\partial z}, \tag{2.1}$$

$$\rho\frac{\partial^2 w_{mass}}{\partial t^2}=\frac{\partial\sigma_{13}}{\partial x}+\frac{\partial\sigma_{23}}{\partial y}+\frac{\partial\sigma_{33}}{\partial z},$$

where $\boldsymbol{u}_{\mathrm{mass}}(\boldsymbol{x},t)=(u_{mass},\ v_{\mathrm{mass}},\ w_{\mathrm{mass}})$ is the displacement field of the mass center of the representative unit cell which contains numerous embedded rigid spheres, ρ is the mass density of the composite and σ_{ij} $(i, j=1, 2, 3)$ is the stresses.

Alternatively, we can rewrite the RHS of eqs.(2.1) in terms of the strains ε_{ij} $(i, j=1, 2, 3)$ through the isotropic linear Hookean law based on the effective elastic constants. Then, the (overall) strain ε of the composite is calculated by the displacement-strain relations of linear elasticity based on the displacement field $\boldsymbol{u}(\boldsymbol{x},t)$ of the composite. Finally, the stresses σ_{ij} $(i, j=1, 2, 3)$ on RHS of eqs.(2.1) can be given in terms of the composite’s displacement field $\boldsymbol{u}(\boldsymbol{x},t)=(u_1, u_2, u_3)$ as

$$\rho\frac{\partial^2 u_{mass}}{\partial t^2}=(\lambda+\mu)\frac{\partial e}{\partial x_1}+\mu\nabla^2 u_1\ ,$$

$$\rho\frac{\partial^2 v_{mass}}{\partial t^2}=(\lambda+\mu)\frac{\partial e}{\partial x_2}+\mu\nabla^2 u_2\ , \tag{2.2}$$

$$\rho\frac{\partial^2 w_{mass}}{\partial t^2}=(\lambda+\mu)\frac{\partial e}{\partial x_3}+\mu\nabla^2 u_3\ ,$$

$$e=\varepsilon_{kk}=\frac{\partial u_1}{\partial x_1}+\frac{\partial u_2}{\partial x_2}+\frac{\partial u_3}{\partial x_3},$$

where (λ, μ) are the effective Lame's elastic constants of the isotropic composite.

In eqs.(2.2), the displacement of the composite $\boldsymbol{u}(\boldsymbol{x},t)$ is also considered as the displacement of the geometrical center of the representative unit cell. So, $\boldsymbol{u}(\boldsymbol{x},t)$ is applied to determining the strain ε caused by the geometrical deformation, while the mass center displacement $\boldsymbol{u}_{\mathrm{mass}}(\boldsymbol{x},t)$ is used on LHS of eqs.(2.1) or (2.2) according to the physical concept of the acceleration based on the center of mass of the body.

In the traditional elastic composite theory, the mass center displacement $\boldsymbol{u}_{\mathrm{mass}}(\boldsymbol{x},t)$ is identical to the geometrical center displacement $\boldsymbol{u}(\boldsymbol{x},t)$, because there is no difference between the displacement field $\boldsymbol{u}_{\mathrm{s}}(\boldsymbol{x},t)$ of embedded rigid spheres and the displacement field $\boldsymbol{u}(\boldsymbol{x},t)$ of the composite. Then, the single displacement field $\boldsymbol{u}(\boldsymbol{x},t)$ is governed by eqs.(2.1) or (2.2) with $\boldsymbol{u}_{\mathrm{mass}}(\boldsymbol{x},t)=\boldsymbol{u}(\boldsymbol{x},t)$. However, for a stiff sphere-reinforced metacomposite characterized by heavy and stiff spheres and soft matrix phase, $\boldsymbol{u}_{\mathrm{mass}}(\boldsymbol{x},t)$ is distinct from $\boldsymbol{u}(\boldsymbol{x},t)$ owing to the deviation ($\boldsymbol{u}$-$\boldsymbol{u}_{\mathrm{s}}$). It is known [12-20] that the deviation ($\boldsymbol{u}$-$\boldsymbol{u}_{\mathrm{s}}$) of the displacement of embedded stiff spheres from the displacement of the composite is responsible for novel dynamic behaviors of the metacomposite. In such case, a key problem is how to get a simple relation between the mass center displacement $\boldsymbol{u}_{\mathrm{mass}}(\boldsymbol{x},t)$ of the representative unit cell and the displacement $\boldsymbol{u}(\boldsymbol{x},t)$ of the composite.

2.1 Relation between $\boldsymbol{u}_{\mathrm{mass}}(\boldsymbol{x},t)$ and $\boldsymbol{u}(\boldsymbol{x},t)$

For this purpose, firstly, let ρ_m be the mass density of the matrix phase and ρ_s be the mass density of the rigid spheres, thus the mass density ρ (per unit volume) of the composite is defined by

$$\rho = \rho_m + (\rho_s - \rho_m)\delta = (1-\delta)\rho_m + \rho_s\delta,\ 0 < \delta < 1, \tag{2.3}$$

where δ is the volume fraction of the embedded rigid spheres.

Then, assume that the average displacement field of the matrix phase is given by the displacement of the composite. And according to the principle of conservation of linear momentum, the mass center displacement $\boldsymbol{u}_{\text{mass}}(\boldsymbol{x},t)$ can be determined by

$$\rho \boldsymbol{u}_{mass} = \rho_m(1-\delta)\boldsymbol{u} + \rho_s\delta\boldsymbol{u}_s\ . \tag{2.4}$$

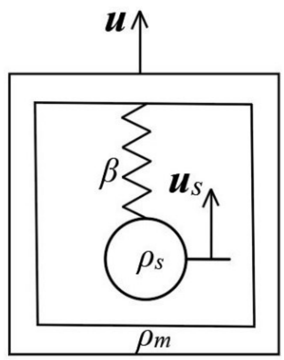

Fig. 2.1 Rigid sphere-spring composite model

(where ρ_m is the mass density of the matrix phase, ρ_s is the mass density of the rigid spheres, $\boldsymbol{u}$ is the displacement field of the composite, $\boldsymbol{u}_s$ is the displacement field of the embedded rigid spheres and β is the spring constant per unit volume of the composite)

Next, consider a representative unit cell containing many randomly distributed identical rigid spheres. Assume that the motion of each rigid sphere can be determined by the interaction (spring) force between the rigid sphere and the surrounding composite [29] which is linearly related to the relative displacement ($\boldsymbol{u}$-$\boldsymbol{u}_s$). So far, our sphere-spring model has been specifically presented (see Fig. 2.1), which is composed of rigid spheres interacting with the surrounding elastic medium through an internal spring force like a spring-mass system in [2]. Let the spring constant for a single rigid sphere embedded within an infinite elastic medium be β_0 (to be specified below, see eq.(2.8)). Then, the equation of motion for the rigid sphere surrounded by the infinite effective medium is governed by the spring constant β>0 (per unit volume of the composite) defined as

$$\beta(\boldsymbol{u} - \boldsymbol{u}_s) = \rho_s \frac{\partial^2 \boldsymbol{u}_s}{\partial t^2}, \beta = \frac{\beta_0}{V_{sphere}} > 0, \tag{2.5}$$

where V_{sphere} is the volume of a single rigid sphere. Eliminating $\boldsymbol{u}_s$ from eqs.(2.4, 2.5), a relation between the mass center displacement $\boldsymbol{u}_{\mathrm{mass}}(\boldsymbol{x},t)$ and the geometrical center displacement $\boldsymbol{u}(\boldsymbol{x},t)$ can be derived as

$$\boldsymbol{u}_{mass} = \boldsymbol{u} - \frac{\rho_s}{\beta}\left(\frac{\partial^2 \boldsymbol{u}_{mass}}{\partial t^2} - \frac{\rho_m}{\rho}(1-\delta)\frac{\partial^2 \boldsymbol{u}}{\partial t^2}\right). \tag{2.6}$$

Therefore, the motion of the rigid sphere-reinforced metacomposite is governed by the well-known classical equations (2.1) or (2.2) coupled with the $\boldsymbol{u}_{\mathrm{mass}}$-$\boldsymbol{u}$ relation (2.6). For instance, an expression for $\boldsymbol{u}_{\mathrm{mass}}$ in terms of $\boldsymbol{u}$ can be obtained by substituting (2.1) or (2.2) into the RHS of (2.6). Alternatively, it follows from the relation (2.6) that

$$\frac{\partial^2 \boldsymbol{u}_{mass}}{\partial t^2} = \frac{\partial^2 \boldsymbol{u}}{\partial t^2} - \frac{\rho_s}{\beta}\left(\frac{\partial^4 \boldsymbol{u}_{mass}}{\partial t^4} - \frac{\rho_m}{\rho}(1-\delta)\frac{\partial^4 \boldsymbol{u}}{\partial t^4}\right). \tag{2.7}$$

Thus the decoupled governing equations for the displacement field $\boldsymbol{u}(\boldsymbol{x},t)$ of the composite can be obtained by substituting $(\boldsymbol{u}_{\mathrm{mass}})_{tt}$ expressed by eqs.(2.1) or (2.2) into both sides of the relation (2.7).

2.2 An expression for the spring constant *β*

Now we need a specific formula of the spring constant β defined for our rigid sphere-spring composite model. For a rigid sphere of radius R embedded in an infinite isotropic linearly elastic medium of (effective) shear modulus (μ) and Poisson ratio (ν), the force F requested for a relative translational displacement Δ of the rigid sphere with respect to the surrounding elastic medium is given by [30, 31]

$$F = \frac{24\pi \Delta R\mu(1-\nu)}{(5-6\nu)} = \frac{12\pi \Delta R\mu}{(q^2+2)}, q = \sqrt{\frac{1-2\nu}{2(1-\nu)}} = \frac{c_2}{c_1}, \tag{2.8}$$

where c_1 and c_2 are the longitudinal and transverse wave speeds of the surrounding (effective) elastic medium, respectively. Thus, because rotation of embedded stiff spheres usually plays a minor role, an expression for the spring constant β defined in eq.(2.5) can be obtained as

$$\beta_0 = \frac{24\pi R\mu(1-\nu)}{(5-6\nu)}, \frac{\beta}{\rho_s} = \frac{18\mu(1-\nu)}{(5-6\nu)\rho_s(R^2)}, \tag{2.9}$$

where (μ, ν) are the effective elastic constants of the isotropic composite, and R is the radius of the embedded rigid spheres.

It is noted that the above eqs. (2.5, 2.8) essentially depend on the assumption of "rigid spheres". If there is no significant difference between the moduli of embedded spheres and matrix, our sphere-spring model would not hold but $\boldsymbol{u}_{\mathrm{mass}}(\boldsymbol{x},t)=\boldsymbol{u}(\boldsymbol{x},t)$ in eqs.(2.1) or (2.2) without the deviation ($\boldsymbol{u}$-$\boldsymbol{u}_{\mathrm{s}}$).

Chapter 3

Effective mass density and the bandgap

In this chapter, we begin with the derivation of effective mass density and bandgap formulas based on our rigid sphere-spring composite model. We will show that rigid spheres embedded in a soft elastic matrix can behave like local resonators, and a rigid sphere-reinforced metacomposite can demonstrate negative effective mass density within a certain range of frequencies. Then, we will apply the derived bandgap formula to several real stiff spherical inclusion reinforced composites and compare our predictions with known data.

3.1 Effective mass density and the bandgap

To define the effective mass density of a rigid sphere-reinforced metacomposite, let us consider a harmonic motion defined by $\boldsymbol{u}_{\text{mass}}(\boldsymbol{x},t)\sim sin\omega t$ and $\boldsymbol{u}(\boldsymbol{x},t)\sim sin\omega t$, where ω is the (circular) frequency. It follows from the above relation (2.6) that

$$\boldsymbol{u}_{mass} = \frac{\left(1 - \frac{\rho_s}{\beta}\frac{\rho_m}{\rho}(1-\delta)\omega^2\right)}{\left(1 - \frac{\rho_s}{\beta}\omega^2\right)}\boldsymbol{u}\,. \tag{3.1}$$

Substitute (3.1) into the eqs. (2.2), and we may obtain

$$\rho\frac{\left(1 - \frac{\rho_s}{\beta}\frac{\rho_m}{\rho}(1-\delta)\omega^2\right)}{\left(1 - \frac{\rho_s}{\beta}\omega^2\right)}\frac{\partial^2\boldsymbol{u}}{\partial t^2} = (\lambda+\mu)\boldsymbol{\nabla}e + +\mu\nabla^2\boldsymbol{u}\,, \boldsymbol{\nabla} = \left(\frac{\partial}{\partial x_1},\frac{\partial}{\partial x_2},\frac{\partial}{\partial x_3}\right), \tag{3.2}$$

where the displacement of the composite $\boldsymbol{u}$=(u_1, u_2, u_3).

According to the general definition of the effective mass density based on the Newton's 2nd law,

$$\rho_{effective}(\omega)\frac{\partial^2\boldsymbol{u}}{\partial t^2} = \boldsymbol{F}_r\,, \tag{3.3}$$

where $\boldsymbol{F}_r$ is the resultant force (per unit volume) acting on the representative unit cell, the effective mass density of a rigid sphere-reinforced metacomposite is given by

$$\rho_{effective} = \rho \frac{\left(1 - \frac{\rho_s}{\beta}\frac{\rho_m}{\rho}(1-\delta)\omega^2\right)}{\left(1 - \frac{\rho_s}{\beta}\omega^2\right)} \,. \tag{3.4}$$

The range of frequency ω within which the effective mass density (3.4) becomes negative, called "bandgap" [ω_0, ω_u], is given by

$$\omega_0^2 < \omega^2 < \omega_u^2 \,, \omega_0^2 = \frac{\beta}{\rho_s} \,, \omega_u^2 = \frac{\beta}{\rho_s}\left(\frac{\rho}{\rho_m(1-\delta)}\right) . \tag{3.5}$$

Actually, in view of the expression (2.9) for the spring constant β, we have

$$\omega_0^2 = \frac{\beta}{\rho_s} = \frac{18\mu(1-\nu)}{(5-6\nu)\rho_s(R^2)} = \frac{9\rho c_1^2}{\rho_s(2q^{-2}+1)R^2} \,, \tag{3.6}$$

where (μ, ν) are the effective elastic constants of the isotropic composite, and R is the radius of the embedded rigid spheres. It is seen from (3.4) that the effective mass density tends to negative infinity when the frequency ω approaches the lower cut-off frequency ω_0 from inside the bandgap. In particular, it is seen from (3.6) that for given effective elastic constants of the composite, the lower cut-off frequency ω_0 is inversely proportional to the radius R of the rigid spheres, which means that the lower cut-off frequency ω_0 approaches infinity when the radius R becomes vanishingly small. Here, it is noted that the above formulas (3.6) for (ω_0^2) and (3.5) for (ω_u^2) reduce to eqs.(2) and (3) of Kinra & Li [14] for dilute inclusion distribution (with the volume fraction δ<<1) when $\rho \approx \rho_m$ and $(c_1)=(c_1)_m$ and $(c_s)=(c_s)_m$.

Here it should be stated that since periodic composites are a special kind of random composites, it is known (see e.g. [17]) that the local resonance at the lower cut-off frequency ω_0, as given by the present model (3.6), dominates for both random and periodic composites and causes similar bandgap with the otherwise identical volume fraction of embedded stiff spheres. For a periodic composite, depending on the mass density ratio and the volume fraction of embedded spheres, the local resonance bandgap can be (most likely) lower than or close to, or (rarely) higher than the lowest Bragg bandgap. And an overlapped bandgap has a more drastic effect on wave propagation as the local resonance bandgap is coincident with or very close to the lowest Bragg bandgap (see e.g. [19]).

In addition, the present effective medium model is limited to the cases when the characteristic wavelength of the composite's displacement field is much larger than the diameter $2R$ of the embedded rigid spheres in the random composite. Clearly, for free and forced vibration of a rigid sphere-reinforced metacomposite of finite dimensions (as discussed in sections 4 & 5), this "long wavelength" condition can usually be met almost without any meaningful restrictions, because the characteristic wavelength of the displacement field is largely determined by the dimensions of the composite which are usually a few orders of magnitude larger than the diameter of embedded rigid spheres (or the lattice constant of periodic composites), e.g., see Chapters 4 & 5. For transient wave propagation in an infinite composite, because the local resonance frequency ω_0 given by (3.6) plays the key role in locally resonant metamaterials, this "long-wavelength" condition requests $(2\pi c/\omega_0)>>(2R)$, where c is the effective sound speed of the composite. Under the present conditions $q\leq 1/2$ and $\rho_s>>\rho_m$, it is seen from (3.6) that $(2\pi c/\omega_0)$ can be a few times larger than $(2R)$ at the local resonance frequency ω_0. Therefore, the "long-wavelength" assumption for the present model can be satisfied at the local resonance frequency ω_0, and the formulas (3.5, 3.6) could be applicable with reasonable accuracy. For example, the experiments [13] for lead-epoxy random composites ($\rho_s/\rho_m\approx 9.5$, with the volume fraction δ=0.05 or 0.1 and different radii of lead spheres, R=0.25mm or 0.66mm) showed that the observed wave propagation is attenuated drastically due to the local resonance around $(\omega R/c_s)\approx 1$, which is very close to the value of ω_0 given by the present model (3.6) with about 10% relative errors. In what follows, let us make more detailed comparison of the bandgap frequencies predicted by the present model (3.5, 3.6) with known data for several typical stiff sphere-reinforced polymer composites.

3.2 Comparison to known data

The present model is characterized by the general 3D $\boldsymbol{u}_{\text{mass}}$-$\boldsymbol{u}$ relation (2.6) and the spring constant formula (2.9). Therefore, for validating the present model, it is relevant to demonstrate the validity and accuracy of the relation (2.6) and the formula (2.9), or eqs.(3.5, 3.6) as their consequences. To demonstrate the validity and accuracy of the present formulas (3.5, 3.6), let us compare their predicted results with some known experimental data and numerical simulations for stiff sphere-reinforced metacomposites.

The effective elastic constants (e.g., the effective Young's and shear moduli E and μ) in our formulas can be determined by the theory of isotropic elastic composites [23, 32-34]. It is indicated in most literatures [23-27, 32-34] that the effective elastic constants of the stiff sphere-reinforced metacomposite are mainly dependent on the volume fraction of the embedded rigid spheres. And the size and specific distribution of the rigid spheres have slight, or even ignorable, influence on the effective elastic moduli of the composite [33, 34]. So, for the simplicity, let us employ the refined Einstein formula (for more detailed discussion, see e.g. [23, 32, 34]) for the effective elastic moduli of rigid sphere-reinforced random metacomposites

$$\frac{E}{E_m} = \frac{\mu}{\mu_m} = 1 + 2.5\delta + 5\delta^2 \,, \tag{3.7}$$

where E_m and μ_m are the Young's and shear moduli of the matrix phase, respectively, and δ is the volume fraction of the rigid spheres. The formulas (3.7) for effective moduli of stiff sphere-reinforced metacomposites are reasonably accurate for the cases when the elastic moduli of embedded spheres are much larger than that of the soft matrix phase and the volume fraction of the embedded spheres is not too high (for instance, not higher than 0.5). From this perspective, eqs.(3.7) are much applicable to our model with the assumption of "rigid spheres". In addition, eqs.(3.7) assumes that the influence of the embedded rigid spheres on the Poisson ratio of the composite can be ignored and the effective Poisson ratio of the composite can be approximated by the Poisson ratio of the matrix phase [23, 32].

a). Steel sphere-reinforced polyester: As the first example, let us consider the steel sphere-reinforced polyester studied by Sainidou et al. [20]. For instance, it is seen from fig.1 of [20] (for face-centered cubic lattice, with δ=0.184 and $R \approx 0.22a_0$) that the simulation values of the (dimensionless) bandgap are $2.32 < \omega a_0/(c_l)_m < 3.23$, where a_0 is the lattice constant, and $(c_l)_m$ is the longitudinal wave speed of the polyester matrix. With the mass densities ρ_s=7800 kg/m^3 for steel and ρ_m=1220 kg/m^3 for polyester, and the transverse and longitudinal wave speeds for the polyester matrix, $(c_s)_m$=1180 m/s and $(c_l)_m$=2490 m/s, respectively, the present formulas (3.5, 3.6) give the bandgap $2.17 < \omega a_0/(c_l)_m < 3.38$, in good agreement with the bandgap (2.32 to 3.23) given in [20] with relative errors less than 10%.

b). Glass sphere-reinforced polyester: As the second example, let us consider the glass sphere-reinforced polyester studied by Maslov & Kinra [18].With the glass mass densities ρ_s=2490 kg/m^3, a comparison between the bandgap predicted by the present model (3.5, 3.6) and the experimental data given in Maslov & Kinra [18] based on the transmission and reflection coefficients (see their figs.10 and 12, where $a \approx 0.56$mm is the radius of glass spheres, and d is the lattice constant) is shown in Table 3.1, where k_p is the longitudinal wave number ($=\omega/(c_l)_\mathrm{m}$) and k_s the transverse wave number ($=\omega/(c_s)_\mathrm{m}$) of the matrix, and $\Omega = k_s d/(2\pi) = \omega d/(2\pi(c_s)_\mathrm{m})$. It is seen from Table 3.1 that the results predicted by the present model are in reasonable agreement with the experimental data of Maslov & Kinra [18] with typical relative errors less than 10% and the maximum relative errors around 25-30%. The most possible immediate cause of the larger errors is the use of area fractions of glass spheres, instead of volume fractions, to compute bandgaps. What is more, the glass sphere-reinforced polyester with only one layer of embedded spheres in [18] cannot be treated as a homogeneous elastic body, which is not equivalent to our model. However, the present model can still provide a reasonably accurate estimation of bandgap even for this composite with stiff spheres merely gathering in a small region within the matrix.

In addition, it is verified from Table 3.1 that the bandgap frequencies for this glass sphere-reinforced polyester composite are within the range of MHz with the radius of spheres $R \approx 0.56$mm.

Table 3.1 Comparison between the present results and the experimental data for a glass sphere polyester composite [18]

Specimens	Present results by Eqs (3.5, 3.6)	Experiments [18]
(a) R/d=0.21, δ=0.14	$0.80 < k_p R < 0.93$ $1.28 < \Omega < 1.48$	$0.63 < k_p R < 0.90$ $1.00 < \Omega < 1.41$
(b) R/d=0.3, δ=0.28	$0.97 < k_p R < 1.29$ $1.08 < \Omega < 1.45$	$0.90 < k_p R < 1.27$ $1.00 < \Omega < 1.41$

c). Lead sphere-reinforced epoxy: As the third example, let us consider the lead sphere-reinforced epoxy studied by Kafesaki et al. [16] characterized by the modulus ratio (of sphere-to-matrix) about 5. For instance, it is seen from fig.1 of [16] (where R is the radius of the lead spheres, with δ=0.262) that the bandgap is $1.5<\omega R/(c_s)_\mathrm{m}<2.0$. With the mass densities ρ_s=11357 kg/m^3 for lead and ρ_m=1180 kg/m^3 for epoxy, and the transverse and longitudinal wave speeds for the epoxy matrix, $(c_s)_\mathrm{m}$=1160 m/s and $(c_l)_\mathrm{m}$=2540 m/s, respectively, the present formulas (3.5, 3.6) give the bandgap $0.92<\omega R/(c_s)_\mathrm{m}<1.93$. For the same case, alternatively, fig.2 of [16] (with R=0.25d, where d is still the lattice constant) gives the bandgap $6.2<(\omega d/(c_s)_\mathrm{m})<7.9$, and our formulas give

$3.68<\omega d/(c_s)_m<7.73$. Therefore, even for the moderately stiff lead spheres embedded in an epoxy matrix (with the modulus ratio around 5), the present model still gives useful results with acceptable relative errors, consistent with a basic conclusion of several previous works [14, 19]. These comparisons confirm the reasonable accuracy of the present simple model for stiff sphere-reinforced random composites provided that the modulus ratio (of sphere-to-matrix) is much larger than unity.

Chapter 4

Vibration and buckling of a rigid sphere-reinforced metacomposite beam

Now let us apply the present model to study vibration and dynamic buckling of a rigid sphere-reinforced metacomposite beam, with an emphasis on the consequences of the negative effective mass density and the bandgap on non-classical dynamic behavior of the composite beam.
The equations (2.2) for the transverse deflection $w(\boldsymbol{x},t)$ of a rigid sphere-reinforced metacomposite (Euler-Bernoulli) beam is of the form

$$\rho A \frac{\partial^2 w_{mass}}{\partial t^2} = -P\frac{\partial^2 w}{\partial x^2} - EI\frac{\partial^4 w}{\partial x^4}\,, \tag{4.1}$$

where w_{mass} is the deflection of the mass center of the representative unit cell, while w is the deflection of the composite beam, ρ is the mass density (per unit volume) of the composite, E is the effective Young's modulus of the composite beam, A and I are the cross-sectional area and the moment of cross-section of the composite beam, and P is the external axial compressive force applied to the beam. Here, it is stated that higher-order beam models have been used in existing literature on dynamics of composite beams, see e.g. a recent work [35] for an analysis of a Timoshenko beam with periodically distributed spring-mass resonators.
Substituting (4.1) into the relation (2.7) gives the $w_{\mathrm{mass}}(\boldsymbol{x},t)$-$w(\boldsymbol{x},t)$ relation

$$w_{mass} = w + \frac{\rho_s}{\beta}\left(\frac{1}{\rho A}\left(P\frac{\partial^2 w}{\partial x^2} + EI\frac{\partial^4 w}{\partial x^4}\right) + \frac{\rho_m}{\rho}(1-\delta)\frac{\partial^2 w}{\partial t^2}\right). \tag{4.2}$$

Thus, the governing equation for the deflection $w(\boldsymbol{x},t)$ of the metacomposite beam is given by

$$P\left(1+\frac{\rho_s}{\beta}\frac{\partial^2}{\partial t^2}\right)\frac{\partial^2 w}{\partial x^2} + EI\left(1+\frac{\rho_s}{\beta}\frac{\partial^2}{\partial t^2}\right)\frac{\partial^4 w}{\partial x^4} + \rho A\left(1+\frac{\rho_s}{\beta}\frac{\rho_m}{\rho}(1-\delta)\frac{\partial^2}{\partial t^2}\right)\frac{\partial^2 w}{\partial t^2} = 0\,, \tag{4.3}$$

which can reduce to the classical elastic composite beam equation when $\beta=\infty$.

4.1 Free vibration of a hinged or cantilever beam

For the free vibration of a hinged beam of length L with P=0, the boundary conditions are $w|_{x=0} =$

$w|_{x=L} = w''|_{x=0} = w''|_{x=L} = 0$. Let us consider the deflection of the form $w(\boldsymbol{x},t)=sin(m\pi x/L)e^{i\omega t}$ (m=1, 2…), where ω is the natural frequency and the integer m is the mode number. Then the above eq.(4.3) gives

$$EI\left(1-\frac{\rho_s}{\beta}\omega^2\right)\left(\frac{m\pi}{L}\right)^4 = \rho A\left(1-\frac{\rho_s}{\beta}\frac{\rho_m}{\rho}(1-\delta)\omega^2\right)\omega^2 \,. \tag{4.4}$$

Let the two natural frequencies for each mode number m (≥1) be (ω_1, ω_2), where $\omega_2 \geq \omega_1$, determined by the following quadratic equation of (ω^2) with P=0,

$$a\omega^4 + b\omega^2 + c = 0\,,\, \omega_{1,2}^2 = \frac{-b \mp \sqrt{b^2-4ac}}{2a} = \left(-\frac{b}{2a}\right)\left(1 \mp \sqrt{1-\frac{4ac}{b^2}}\right), \tag{4.5}$$

where

$$a = \frac{A\rho_s\rho_m(1-\delta)}{\beta} > 0\,,\, b = -\left(EI\frac{\rho_s}{\beta}\left(\frac{m\pi}{L}\right)^4 + \rho A\right) < 0\,,\, c = EI\left(\frac{m\pi}{L}\right)^4 > 0\,. \tag{4.6}$$

Since $\rho \geq \rho_m(1\text{-}\delta)$, it follows that

$$\left(EI\frac{\rho_s}{\beta}\left(\frac{m\pi}{L}\right)^4 + \rho A\right)^2 \geq 4\frac{A\rho_s\rho_m(1-\delta)}{\beta}\left[EI\left(\frac{m\pi}{L}\right)^4\right]. \tag{4.7}$$

Thus, we have $b^2 \geq 4ac$, and the two roots (ω^2) of (4.5) are always strictly positive. In addition, it can be verified that the two roots (ω^2) of eq.(4.5), as a function of the mode number m, have no stationary point at any finite value of m, and actually the two roots (ω^2) of eq.(4.5) both increase with the integer m. Therefore, the larger natural frequency ω_2 for any integer m (m≥1) is bounded from below by its limit value at m=0 which is equal to the upper cut-off frequency of the bandgap given by

$$\omega_2^2 > \omega_u^2 = \omega_0^2\left(\frac{\rho}{\rho_m(1-\delta)}\right), m \geq 1\,. \tag{4.8}$$

On the other hand, the upper limit of the smaller natural frequency ω_1 can be obtained by eq.(4.5) with m=∞ which is equal to the lower cut-off frequency of the bandgap as

$$\omega_1^2 \leq \omega_0^2\,, m \geq 1\,. \tag{4.9}$$

In conclusion, the natural frequencies of the hinged rigid sphere-reinforced metacomposite beam for any integer m ($m \geq 1$) always stay outside of the bandgap $[\omega_0, \omega_u]$ defined by (3.5), independent of all other material and geometrical parameters, consistent with the physical concept of the "bandgap". Similar phenomenon is common in metamaterial beams with local resonance, see e.g. [36] for an analysis on the two branches of natural frequencies of an elastic beam with distributed spring-mass resonators. Here, as an example, natural frequencies of a hinged steel-sphere polyester composite beam are shown in Fig. 4.1 for different volume fractions of the steel spheres. There are two separate curves with a bandgap in Fig. 4.1, unlike a traditional elastic beam whose natural frequency as a function of the mode number m is a single monotonically increasing curve without bandgap. It is seen from Fig. 4.1 that with the given radius of rigid spheres, both the lower and upper cut-off frequencies ω_0 and ω_u increase with the volume fraction of the rigid spheres, consistent with the experimental data of [17, 18] (also see Table 3.1 of the present thesis). In particular, it is captured from Fig. 4.1 that the wavelength ($2L/m$) of the free vibration modes of the cm-sized composite beam are much larger than ($2R$) and the lattice constant for, say, the lowest-order 50 modes ($m \leq 50$), which justifies the "long-wavelength" condition for the present model.

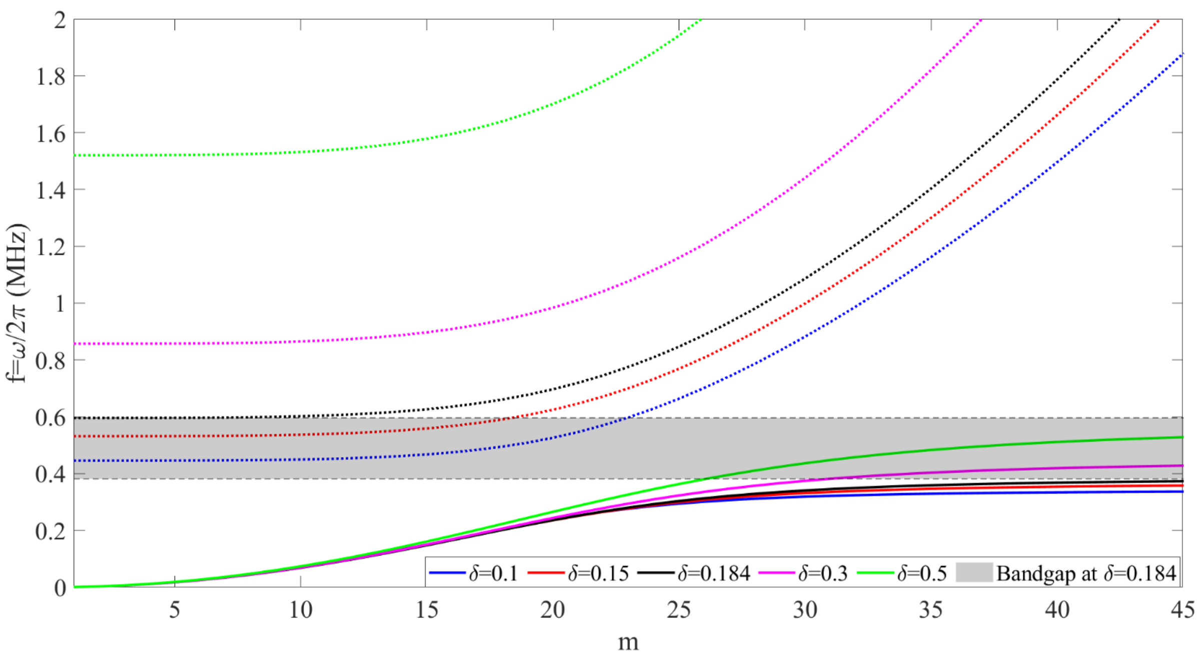

Fig. 4.1 Natural frequencies ($f=\omega/2\pi$) of a hinged steel sphere-polyester composite beam, as a function of the mode number m for different volume fractions, of a circular cross-section with the diameter D=1cm, the length L=10D, and the radius of steel spheres R=0.5 mm, where ρ_s= 7800 kg/m^3, ρ_m= 1220 kg/m^3, $(c_s)_m$=1180 m/s and $(c_l)_m$=2490 m/s

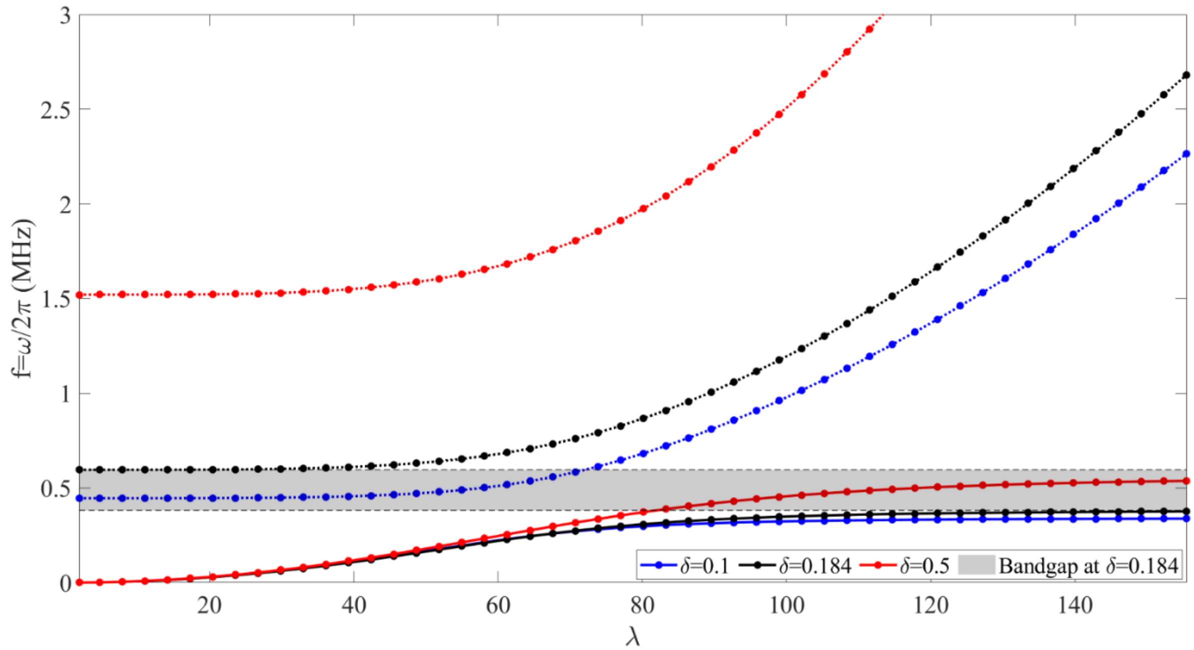

Fig. 4.2 Natural frequencies of a steel sphere-polyester composite cantilever beam, as a function of λ for different volume fractions, of a circular cross-section with the diameter D=1cm, the length L=10D, and the radius of steel spheres R=0.5 mm, where ρ_s= 7800 kg/m^3, ρ_m= 1220 kg/m^3, $(c_s)_m$=1180 m/s and $(c_l)_m$=2490 m/s

Next, let us discuss the free vibration of a rigid sphere-reinforced metacomposite cantilever beam of length L with P=0. Based on the boundary conditions $w|_{x=0} = w'|_{x=0} = w''|_{x=L} = w'''|_{x=L} = 0$, the deflection for the cantilever becomes as (see eq.(9) in [37])

$$w(x,t) = W_m(x)e^{i\omega t},$$

$$W_m(x) = \frac{sin\,\lambda_m - sinh\,\lambda_m}{cos\,\lambda_m + cosh\,\lambda_m}\left(sin\frac{\lambda_m x}{L} - sinh\frac{\lambda_m x}{L}\right) + \left(cos\frac{\lambda_m x}{L} - cosh\frac{\lambda_m x}{L}\right),$$

$$cos\,\lambda_m\,cosh\,\lambda_m = -1\,, \tag{4.10}$$

where the constants λ_1= 1.875, λ_2= 4.694, and $\lambda_m \approx (2m\text{-}1)\,\pi/2$ for $m \geq 3$ (m=1, 2…) [38, 39]. Thus, after substituting $w(\boldsymbol{x},t)$ for the cantilever into the above eq.(4.3), it is given

$$EI\left(1 - \frac{\rho_s}{\beta}\omega^2\right)\left(\frac{\lambda_m}{L}\right)^4 = \rho A\left(1 - \frac{\rho_s}{\beta}\frac{\rho_m}{\rho}(1-\delta)\omega^2\right)\omega^2 \tag{4.11}$$

so that the coefficients, a, b and c, in eq.(4.5) are as follows:

$$a = \frac{A\rho_s\rho_m(1-\delta)}{\beta} > 0\,, b = -\left(EI\frac{\rho_s}{\beta}\left(\frac{\lambda_m}{L}\right)^4 + \rho A\right) < 0\,, c = EI\left(\frac{\lambda_m}{L}\right)^4 > 0\,. \tag{4.12}$$

Obviously, b^2-$4ac \geq 0$ still holds, and the two roots (ω^2) are positive for the cantilever beam. Fig. 4.2 exhibits natural frequencies of a steel-sphere polyester composite cantilever beam, which are also two sets of curves separated by the bandgap. The two roots (ω^2) increase with λ_m without any stationary point, however, they are bounded by the lower and upper cut-off frequency, ω_0 and ω_u, as well. As a result, the bandgap behavior of the cantilever is like that of the hinged beam, where ω_0 and ω_u are consistent with the experimental data of [20] at δ=0.184.

4.2 Dynamic buckling of a hinged beam

Now let us examine the implications of the effective mass density to buckling behavior of a hinged stiff sphere-reinforced metacomposite beam under a constant compressive force P>0. It is well known that dynamic and static criteria give exactly same critical buckling load for a classical elastic beam under such a constant (dead) compressive load. Here, it is of interest to examine if the frequency-dependent effective dynamic mass density, discussed in section 3.1, could change this conclusion for a rigid sphere-reinforced metacomposite beam. For dynamic buckling of a hinged beam of length L, let us consider the deflection of the form $w(\boldsymbol{x},t)=sin(m\pi x/L)e^{i\omega t}$ (m=1,2…) for which the eq.(4.3) gives

$$EI\left(1-\frac{\rho_s}{\beta}\omega^2\right)\left(\frac{m\pi}{L}\right)^4 - \rho A\left(1-\frac{\rho_s}{\beta}\frac{\rho_m}{\rho}(1-\delta)\omega^2\right)\omega^2 = P\left(1-\frac{\rho_s}{\beta}\omega^2\right)\left(\frac{m\pi}{L}\right)^2\,. \tag{4.13}$$

Thus, the eigen-equation for (ω^2) with P>0 is given by

$$a\omega^4 + b\omega^2 + c = 0\,, \tag{4.14}$$

where

$$a = \frac{A\rho_s\rho_m(1-\delta)}{\beta} > 0, b = \left(P\frac{\rho_s}{\beta}\left(\frac{m\pi}{L}\right)^2 - EI\frac{\rho_s}{\beta}\left(\frac{m\pi}{L}\right)^4 - \rho A\right),$$

$$c = EI\left(\frac{m\pi}{L}\right)^4 - P\left(\frac{m\pi}{L}\right)^2. \tag{4.15}$$

It is clear that the N&S condition for dynamic stability of the compressed composite beam is that the two roots of (ω^2) must be non-negative real numbers ($\omega^2 \geq 0$), which are equivalent to

$$b \leq 0\,, c \geq 0\,, b^2 \geq 4ac\,, \tag{4.16}$$

or, equivalently

$$\rho A \geq \left[P - EI\left(\frac{m\pi}{L}\right)^2\right]\left(\frac{m\pi}{L}\right)^2,$$

$$EI\left(\frac{m\pi}{L}\right)^2 \geq P\,, \tag{4.17}$$

$$\left(EI\frac{\rho_s}{\beta}\left(\frac{m\pi}{L}\right)^4 - P\frac{\rho_s}{\beta}\left(\frac{m\pi}{L}\right)^2 + \rho A\right)^2 \geq 4\frac{A\rho_s\rho_m(1-\delta)}{\beta}\left[EI\left(\frac{m\pi}{L}\right)^4 - P\left(\frac{m\pi}{L}\right)^2\right].$$

Note that

$$\left(EI\frac{\rho_s}{\beta}\left(\frac{m\pi}{L}\right)^4 - P\frac{\rho_s}{\beta}\left(\frac{m\pi}{L}\right)^2 - \rho A\right)^2 \geq 0\,, \rho \geq \rho_m(1-\delta)\,, \tag{4.18}$$

it is verified that the 2nd condition of (4.17) implies that

$$\left(EI\frac{\rho_s}{\beta}\left(\frac{m\pi}{L}\right)^4 - P\frac{\rho_s}{\beta}\left(\frac{m\pi}{L}\right)^2 + \rho A\right)^2 \geq 4A\rho\left(\frac{\rho_s}{\beta}\right)\left[EI\left(\frac{m\pi}{L}\right)^4 - P\left(\frac{m\pi}{L}\right)^2\right]$$

$$\geq 4\frac{A\rho_s\rho_m(1-\delta)}{\beta}\left[EI\left(\frac{m\pi}{L}\right)^4 - P\left(\frac{m\pi}{L}\right)^2\right]. \tag{4.19}$$

Therefore, it is concluded that the listed 3 conditions (4.17) are always met provided the 2nd one of (4.17) is met. Thus, the stability condition is given by the 2nd condition (which is identical to the well-known classical critical condition) as follows

$$EI\left(\frac{\pi}{L}\right)^2 \geq P\,, (m = 1). \tag{4.20}$$

Therefore, the effective dynamic mass density gives exactly the same critical buckling load as the classical static criterion for a rigid sphere-reinforced metacomposite beam. On the other hand, when the critical condition (4.20) with m=1 is met, it is seen from (4.15) that c=0 and one of the two roots (ω^2) of eq.(4.14) is zero and the other non-zero root (ω^2) of eq.(4.14) is the upper cut-off frequency given by

$$\omega_u^2 = \frac{\beta}{\rho_s}\left(\frac{\rho}{\rho_m(1-\delta)}\right). \tag{4.21}$$

The deflection ratio w/w_{mass} corresponding to the critical condition (4.20) is determined by eq.(4.1), which gives $\partial w_{\text{mass}}/\partial t=0$. Thus, it follows from (2.4) that the deflection ratio w/w_{s} (of composite-to-sphere) corresponding to the critical condition (4.20) is given by

$$\frac{w}{w_s} = \frac{-\rho_s \delta}{\rho_m(1-\delta)} = \frac{-M_s}{M_m}\,. \tag{4.22}$$

where (M_s/M_m) is the mass ratio of the rigid-sphere phase to the matrix phase. It is concluded that when the buckling is initiated at the critical state determined by the condition (4.20), the sign of the deflection of the embedded rigid spheres is opposite to the sign of the deflection of the composite beam, and their deflection ratio is inversely proportional to their mass ratio. In particular, when the mass ratio (M_s/M_m) of the rigid-sphere phase to the matrix phase is vanishingly small, the buckling is characterized by the localized deflection of the embedded rigid spheres while the displacement of the composite remains vanishingly small, a phenomenon somewhat similar to "local buckling" discussed in the literature (see e.g. [40, 41]). This result distinguishes the present metamaterial beam model from the classical composite beam model, the latter ignores the jump $(\boldsymbol{u}_{\text{mass}}-\boldsymbol{u})$ between the displacement of embedded rigid spheres and the displacement of the composite beam and then $\partial w_{\text{mass}}/\partial t=0$ implies $\partial w/\partial t=0$.

4.3 Forced vibration driven by vibrating ends

In this section, we will analyze the forced vibration of a rigid sphere-reinforced metacomposite hinged or cantilever beam under vibrating ends through eq.(4.3) combined with the relevant boundary conditions.

4.3.1 A hinged beam with two vibrating ends [42, 43]

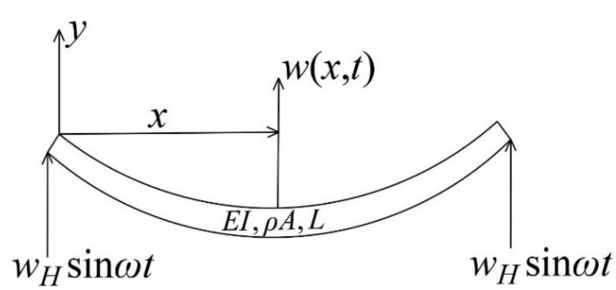

Fig. 4.3 A schematic diagram of a hinged beam driven by two vibrating ends

Firstly, let us consider a hinged rigid sphere-reinforced metacomposite beam of length L driven by two identical harmonically vibrating ends at x=0 & x=L with P=0 (shown as Fig. 4.3). Thus, we have

$$EI\left(1+\frac{\rho_s}{\beta}\frac{\partial^2}{\partial t^2}\right)\frac{\partial^4 w}{\partial x^4}+\rho A\left(1+\frac{\rho_s}{\beta}\frac{\rho_m}{\rho}(1-\delta)\frac{\partial^2}{\partial t^2}\right)\frac{\partial^2 w}{\partial t^2}=0\,,$$

$$w|_{x=0}=w|_{x=L}=w_H\sin\omega t\,, w''|_{x=0}=w''|_{x=L}=0, \tag{4.23}$$

where w_H is the amplitude of the vibrating ends. Then, the stimulated steady state forced vibration of the hinged rigid sphere-reinforced metacomposite beam is of the form

$$w(x,t)=f(x)\sin\omega t\,, f(x)=w_H\left(1+\sum_{k=1}^{\infty}a_k\sin\frac{k\pi x}{L}\right), \tag{4.24}$$

where a_k (k = 1,2,3, ⋯) are some real constants. Substituting (4.24) into eq.(4.23), and using the Fourier series expansion

$$1=\sum_{k=1}^{\infty}\frac{2[1-\cos(k\pi)]}{k\pi}\sin\frac{k\pi x}{L}\,, 0\le x\le L\,, \tag{4.25}$$

we can obtain

$$a_k=\frac{\rho A\omega^2\left(1-\frac{\rho_s}{\beta}\frac{\rho_m}{\rho}(1-\delta)\omega^2\right)\frac{2[1-\cos(k\pi)]}{k\pi}}{EI\left(1-\frac{\rho_s}{\beta}\omega^2\right)\left(\frac{k\pi}{L}\right)^4-\rho A\left(1-\frac{\rho_s}{\beta}\frac{\rho_m}{\rho}(1-\delta)\omega^2\right)\omega^2}\,. \tag{4.26}$$

Substituting eq.(4.26) into (4.24), the forced vibration of the hinged rigid sphere-reinforced metacomposite beam driven by two vibrating ends can be evaluated, as detailed in Section 4.3.2.

To the best of our knowledge, relevant data for hinged particle-reinforced metamaterial beams driven by vibrating ends are unavailable, thus verification of the above eq.(4.24) with (4.26) by comparing with known data fails to proceed. However, the methodology applied here can be found in existing literature. For example, our eq.(4.24) and the above Fourier series expansion (4.25) are of the same form as eqs. (14) & (15) of [42] or (9) & (10) of [43]. The derived eq.(4.24) with (4.26) thus are valid to some extent and applicable in our study to estimate the forced vibration of the hinged composite beam.

4.3.2 Vibration isolation of a hinged beam

It is known that vibration isolation is one of the most remarkable physical phenomena of metamaterials [43-45] which could find significant application to practical problems. Here, we investigate the vibration isolation of a hinged steel sphere-polyester composite beam driven by two vibrating ends based on the above formulas (4.24, 4.26). We consider three cases: (a) excitation frequency lower than the bandgap, (b) excitation frequency within the bandgap, and (c) excitation frequency higher than the bandgap. Through eqs.(3.5, 3.6), we calculate the bandgap of the steel sphere-polyester composite with the volume fraction δ=0.184 and other material parameters given in [20] as (ω_0, 1.56ω_0) equal to that shown in Fig. 4.1.

Then, the forced vibration modes of a hinged steel sphere-polyester composite beam driven by its two vibrating ends are plotted in Fig. 4.4. It is easy to find in Fig. 4.4(b) that when the excitation frequency falls within the bandgap, the forced vibration is highly localized near two vibrating ends while vanishingly small in other parts, which is a typical phenomenon of metamaterials called "vibration isolation" [43-45]. On the contrary, the forced vibration under excitation frequencies out of the bandgap spreads into the entire beam as shown in Fig. 4.4(a) & (c). Additionally, it is seen from Fig. 4.4(a) & (c) that the wavelength of the forced vibration periodic modes is much larger than (2R), which meets the "long-wavelength" condition.

Next, let us study the dependence of the width of the localized vibrational mode on the length of the hinged beam under the excitation frequency within the bandgap. Thereby, the forced vibrational modes of a hinged beam of various lengths driven by two vibrating ends within the bandgap are exhibited in Fig. 4.5. It can be observed from Fig. 4.5 that, for a given bandgap frequency, the width of the localized mode at each vibrating end is almost constant, about 0.6D. Thus, the width of the localized mode is independent of the length of the hinged rigid sphere-reinforced metacomposite beam driven by its two vibrating ends.

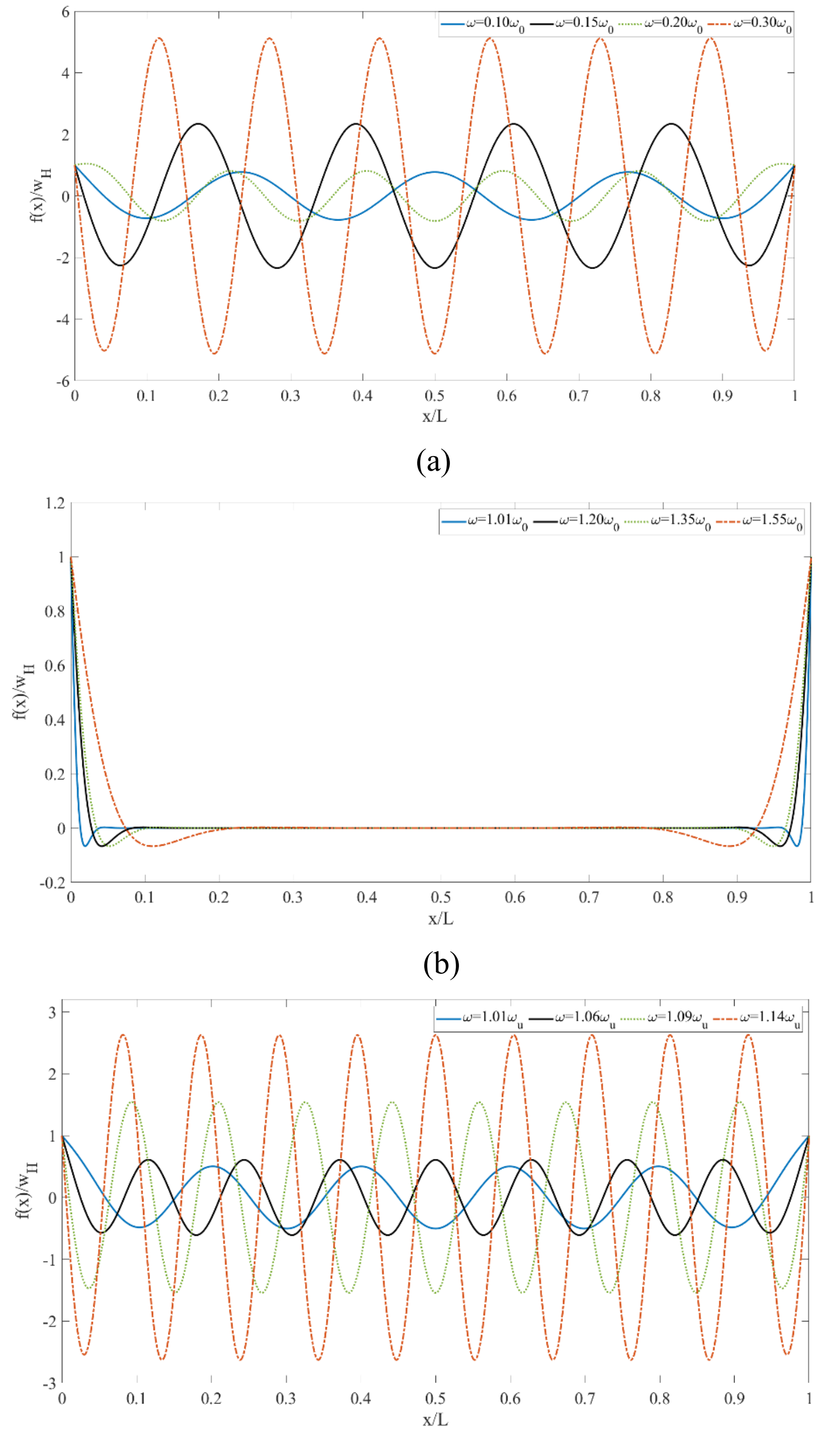

Fig. 4.4 Forced vibration mode of a hinged steel sphere-polyester composite beam driven by two vibrating ends under different excitation frequencies ω: (a) $\omega < \omega_0$, (b) $\omega_0 < \omega < \omega_u$ and (c) $\omega > \omega_u$, where D=1cm, L=10D, R=0.5 mm, ρ_s= 7800 kg/m^3, ρ_m= 1220 kg/m^3, $(c_s)_m$=1180 m/s, $(c_l)_m$=2490 m/s and δ=0.184

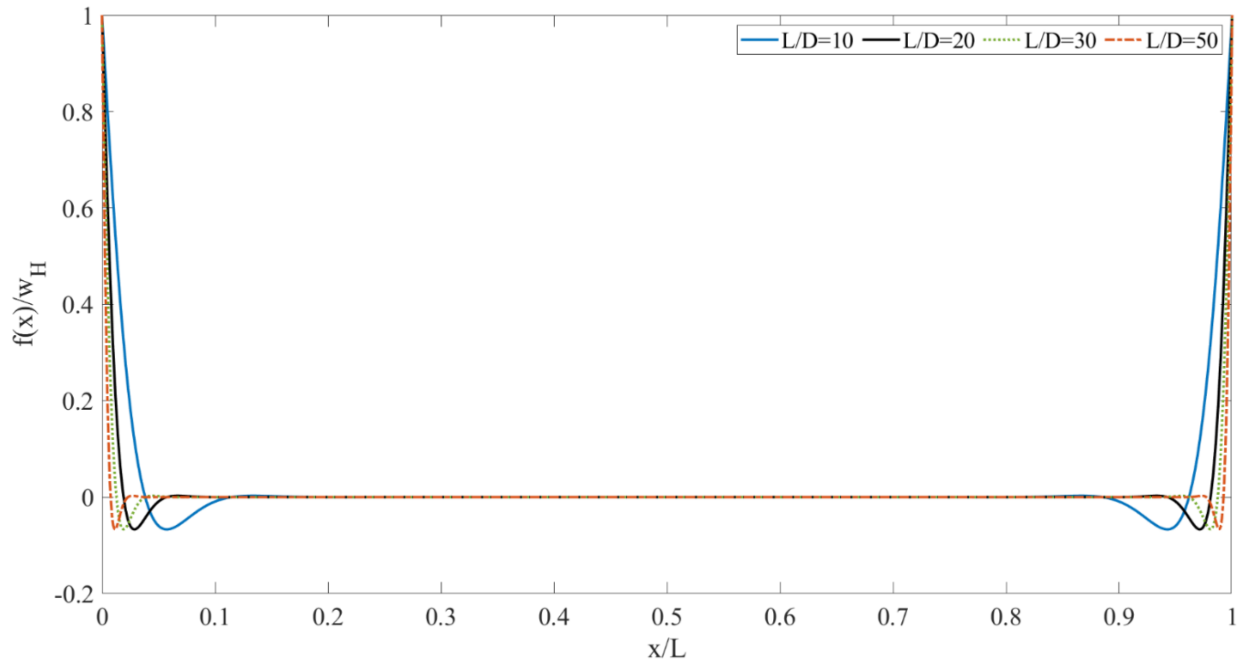

Fig. 4.5 Forced vibrational mode of a hinged steel sphere-polyester composite beam driven by two vibrating ends with different length-to-diameter ratio, where ω=0.90ω_u, D=1cm, R=0.5 mm, ρ_s= 7800 kg/m^3, ρ_m= 1220 kg/m^3, $(c_s)_m$=1180 m/s, $(c_l)_m$=2490 m/s and δ=0.184

4.3.3 A cantilever beam with a vibrating built-in end

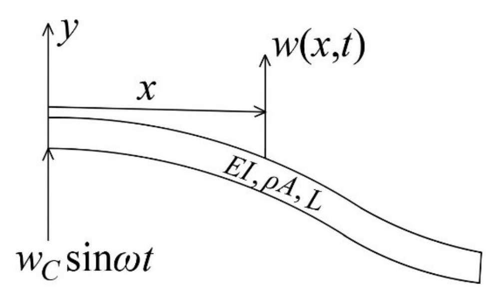

Fig. 4.6 A schematic diagram of a cantilever beam driven by a vibrating built-in end

Next, let us analyze the forced vibration of a rigid sphere-reinforced metacomposite cantilever beam of length L with a vibrating built-in end at $x=0$ (shown as Fig. 4.6), which means

$$w|_{x=0} = w_C \sin \omega t \,, w'|_{x=0} = w''|_{x=L} = w'''|_{x=L} = 0, \qquad (4.27)$$

where w_C is the amplitude of the vibrating built-in end. Thus, the stimulated steady state forced vibration of the rigid sphere-reinforced composite cantilever beam is of the form (see eq.(9) in [37])

$$w(x,t) = f(x)\sin\omega t,$$

$$f(x) = w_C\left(1 + \sum_{k=1}^{\infty} b_k\varphi_k\right),$$

$$\varphi_k = \frac{sin\,\lambda_k - sinh\,\lambda_k}{cos\,\lambda_k + cosh\,\lambda_k}\left(sin\frac{\lambda_k x}{L} - sinh\frac{\lambda_k x}{L}\right) + \left(cos\frac{\lambda_k x}{L} - cosh\frac{\lambda_k x}{L}\right), \tag{4.28}$$

$$cos\,\lambda_k\, cosh\,\lambda_k = -1\,,$$

where b_k and λ_k (k = 1,2,3, ⋯) are some real constants, and λ_1= 1.875, λ_2= 4.694 and $\lambda_k \approx (2k\text{-}1)\,\pi/2$ for $k \geq 3$ [38, 39]. Substituting (4.28) into eq.(4.3) with P=0, and since the mode shape $\varphi_k(x)$ satisfies the orthogonality condition (see eq.(11) in [37]) and its integral is demonstrated as follows:

$$\int_0^L \varphi_k\varphi_m\,dx = L\delta_{km}\,,\int_0^L \varphi_k\,dx = \frac{2L}{\lambda_k}\frac{sin\,\lambda_k - sinh\,\lambda_k}{cos\,\lambda_k + cosh\,\lambda_k}\,, \tag{4.29}$$

where δ_{km} (k, m = 1,2,3, ⋯) is the Kronecker delta, we can obtain

$$b_k = \frac{\rho A\omega^2\left(1 - \frac{\rho_s}{\beta}\frac{\rho_m}{\rho}(1-\delta)\omega^2\right)\frac{2}{\lambda_k}\frac{sin\,\lambda_k - sinh\,\lambda_k}{cos\,\lambda_k + cosh\,\lambda_k}}{EI\left(1 - \frac{\rho_s}{\beta}\omega^2\right)\left(\frac{\lambda_k}{L}\right)^4 - \rho A\left(1 - \frac{\rho_s}{\beta}\frac{\rho_m}{\rho}(1-\delta)\omega^2\right)\omega^2}\,. \tag{4.30}$$

Substituting eq.(4.30) into (4.28), the forced vibration of the rigid sphere-reinforced metacomposite cantilever beam driven by a vibrating built-in end can be evaluated, as detailed in Section 4.3.4.

Now let us validate the above formulas (4.28, 4.30) by comparing with the known data for a metamaterial cantilever beam consisting of lead spheres coated with rubber in an epoxy matrix shown as fig. 1 of [46]. From our eq.(4.28) and the eq.(24) of [46], the transmission coefficient can be computed as

$$T(\omega) = 20\,\lg\frac{f(L)}{w_C}\,. \tag{4.31}$$

However, an additional silicon rubber coating distinguishes the metamaterial beam studied in [46] from our model. So only a qualitative comparison is available here rather than the quantitative comparison like what we did in our Section 3.2. Since the elastic modulus of the coating is much lower than that of the matrix, our eq.(2.9) cannot give an accurate spring constant β_0 for this case. Instead, we may evaluate β_0 according to its definition and the common Hooke's Law as

$$\frac{1}{\beta_0} = \int_{R_1}^{R_2} \frac{1}{E_r(4\pi r^2)} dr \Rightarrow \beta_0 = \frac{4\pi E_r R_1 R_2}{R_2 - R_1}, \beta = \frac{\beta_0}{V_{sphere}} = \frac{3E_r R_2}{(R_2 - R_1){R_1}^2}, \tag{4.32}$$

where E_r is the Young's modulus of silicon rubber coating (=1.078×10^5 Pa), and R_1 & R_2 are respectively the inside and outside radius of the layer of rubber coating (R_1=3mm, R_2=3.5mm) [46]. With the given material and geometric parameters in [46] and some other formulas in our previous chapters, the present formulas (4.28, 4.30) give the result as shown in Fig. 4.7. It is found that the shape of our curve resembles that in fig. 4(a) of [46] despite different resonance frequencies. Thus, the result predicted by our model is in qualitative agreement with the data given by [46], which confirms the reasonable validity of our formulas (4.28, 4.30).

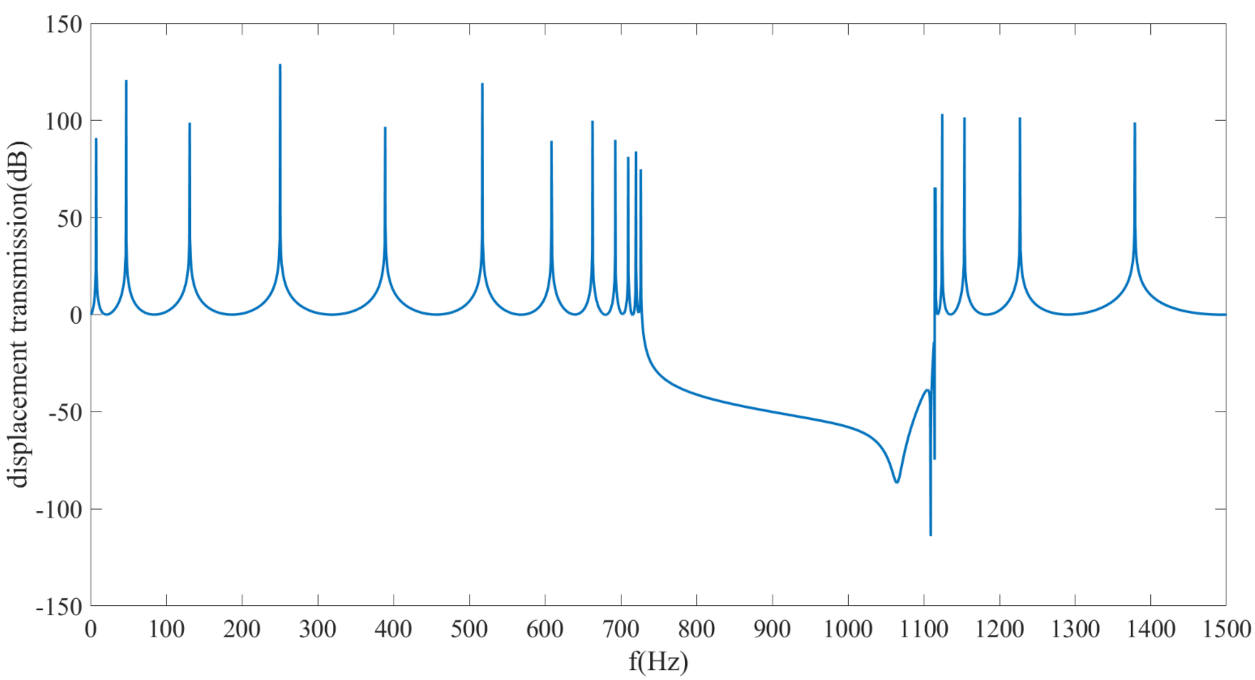

Fig. 4.7 Transmission coefficient of the metamaterial cantilever beam [46] consisting of lead spheres, silicon rubber coating and epoxy matrix under different excitation frequencies, where L=1 m, A=300 mm^2, I=22500 mm^4, R=3 mm, ρ_s= 11600 kg/m^3, ρ_m= 1180 kg/m^3, E_m=4.252×10^9 Pa and δ=0.113

4.3.4 Vibration isolation of a cantilever beam

The vibration isolation of a steel sphere-polyester composite cantilever beam driven by a vibrating built-in end is presented in Fig. 4.8 based on formulas (4.28, 4.30). Here, we still consider three cases of the excitation frequency: (a) lower than the bandgap, (b) within the bandgap, and (c) higher than the bandgap.

For the case within the bandgap in Fig. 4.8(b), forced vibration modes of the cantilever beam are also highly localized near the vibrating end and vanishingly small in other sites except the tiny fluctuations near the free end. However, the trivial waves near the free end might vanish as the excitation frequency approaches the upper cut-off frequency ω_u, say, at ω=1.55ω_0 in Fig. 4.8(b). When the excitation frequency is out of the bandgap, forced vibration modes in Fig. 4.8(a) & (c) spread into the entire beam, though, with irregularity and attenuation near the free end. And the vibrational waves could be more periodic and less weakened at lower excitation frequencies in either Fig. 4.8(a) or (c). Besides, the wavelength of the periodic waves in Fig. 4.8(a) & (c) is still much larger than (2R), which confirms the "long-wavelength" application of the present model. In a word, the vibration isolation phenomenon is visible on a rigid sphere-reinforced metacomposite cantilever beam driven by a vibrating built-in end at bandgap frequencies.

Let us also check whether the width of the localized mode at a given bandgap frequency is related to the length of the metacomposite cantilever beam. Fig. 4.9 depicts the forced vibrational modes of a steel sphere-polyester composite cantilever beam with different lengths driven by a vibrating built-in end within the bandgap. We may find from Fig. 4.9 that the width of the localized mode near the vibrating built-in end is approximately equal to 0.7D. Consequently, the width of the localized mode is independent of the length of a rigid sphere-reinforced metacomposite cantilever beam driven by a vibrating built-in end.

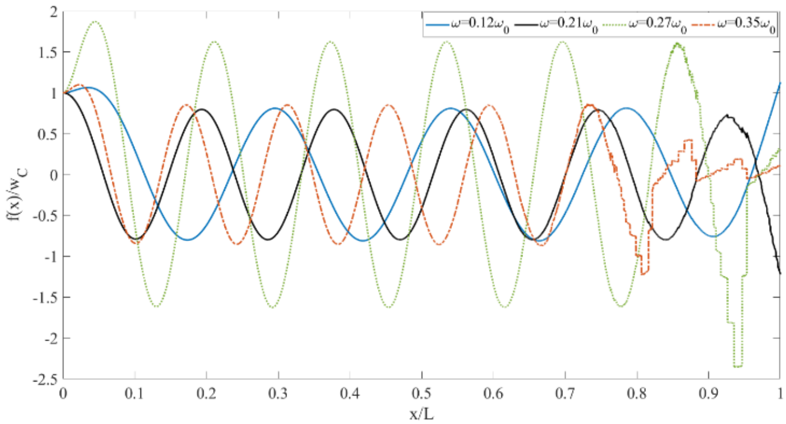

(a)

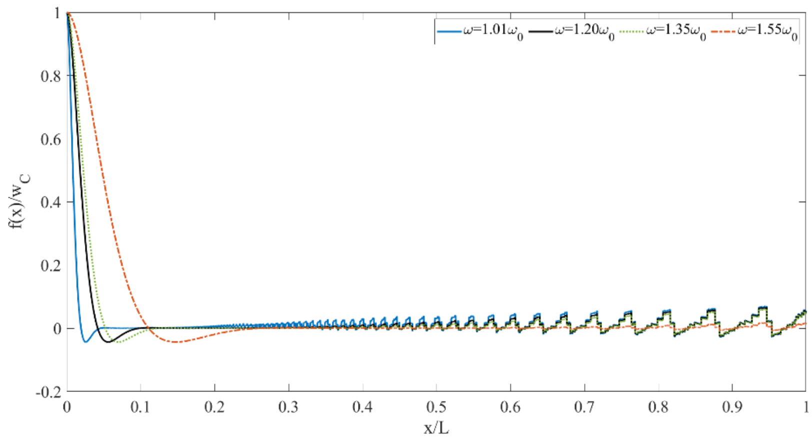

(b)

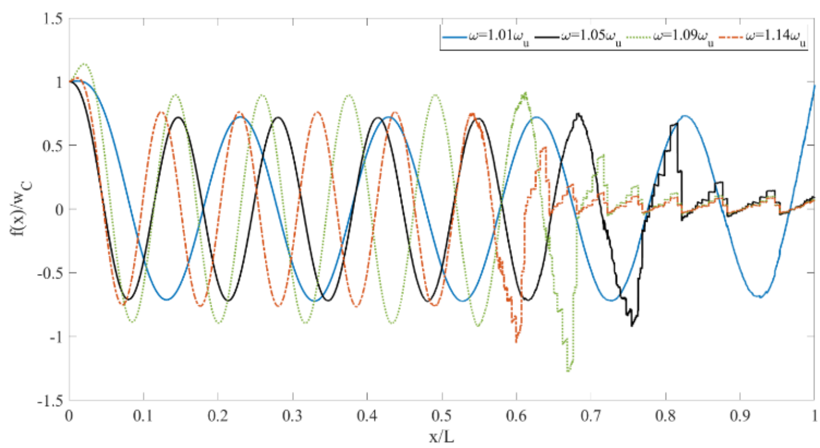

(c)

Fig. 4.8 Forced vibration mode of a steel sphere-polyester composite cantilever beam driven by a vibrating built-in end under different excitation frequencies ω: (a) $\omega < \omega_0$, (b) $\omega_0 < \omega < \omega_u$ and (c) $\omega > \omega_u$, where D=1cm, L=10D, R=0.5 mm, ρ_s= 7800 kg/m^3, ρ_m= 1220 kg/m^3, $(c_s)_m$=1180 m/s, $(c_l)_m$=2490 m/s and δ=0.184

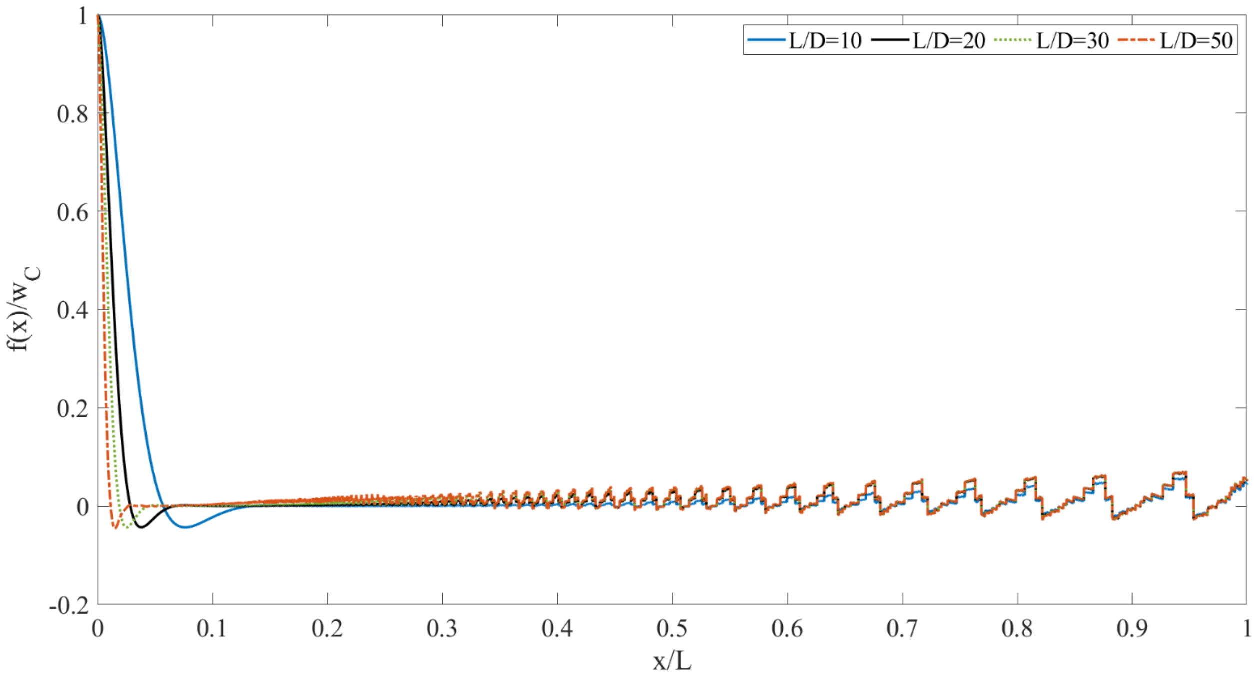

Fig. 4.9 Forced vibrational mode of a steel sphere-polyester composite cantilever beam driven by a vibrating built-in end with different length-to-diameter ratio, where ω=0.90ω_u, D=1cm, R=0.5 mm, ρ_s= 7800 kg/m^3, ρ_m= 1220 kg/m^3, $(c_s)_m$=1180 m/s, $(c_l)_m$=2490 m/s and δ=0.184

4.4 Forced vibration of a hinged beam driven by an external harmonic force [42, 43]

4.4.1 Forced vibration driven by a point force at midway

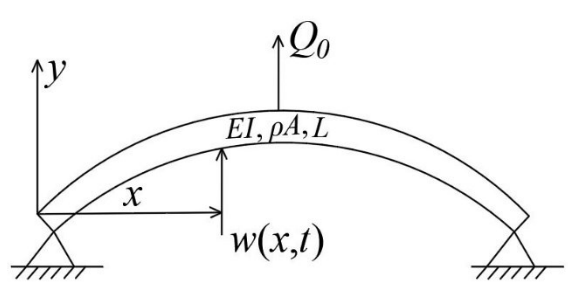

Fig. 4.10 A schematic diagram of a hinged beam driven by a point force at midway

Let us consider an external harmonic force $q(x,t)=q(x)sin\omega t$ applied on a hinged rigid sphere-reinforced metacomposite beam, and so the transverse deflection is governed by the equation

$$\rho A \frac{\partial^2 w_{mass}}{\partial t^2} = -P\frac{\partial^2 w}{\partial x^2} - EI\frac{\partial^4 w}{\partial x^4} + q(x,t)\,. \tag{4.33}$$

The external force $q(x)$ can always be expanded as

$$q(x) = \sum_{k=1}^{\infty} Q_k \sin\frac{k\pi x}{L}\,, \tag{4.34}$$

where Q_k is the Fourier coefficient.

For example, for a point force Q_0 applied at the midway, $x=L/2$, of the hinged beam (see Fig. 4.10),

$$Q_k = \frac{2}{L} Q_0 \sin\frac{k\pi}{2}\,, (k = 1, 2, 3 \dots\dots). \tag{4.35}$$

At this time, the steady-state forced vibration of a hinged rigid sphere-reinforced metacomposite beam can be given by

$$w(x,t) = f(x)\sin\omega t\,, f(x) = \sum_{k=1}^{\infty} c_k \sin\frac{k\pi x}{L}\,, \tag{4.36}$$

where c_k ($k = 1,2,3, \cdots$) are some real constants. Substituting (4.33, 4.34) and (4.36) into the relation (2.7) with P=0, the coefficients c_k are computed as

$$c_k = \frac{\left(1 - \frac{\rho_s}{\beta}\omega^2\right) Q_k}{EI\left(1 - \frac{\rho_s}{\beta}\omega^2\right)\left(\frac{k\pi}{L}\right)^4 - \rho A\left(1 - \frac{\rho_s}{\beta}\frac{\rho_m}{\rho}(1-\delta)\omega^2\right)\omega^2}\,. \tag{4.37}$$

Substituting eq.(4.37) into (4.36), the forced vibration of the hinged rigid sphere-reinforced metacomposite beam driven by a point force applied at its midpoint can be evaluated, as detailed in Section 4.4.2.

To the best of our knowledge, no relevant data is available for a comparison concerning the forced vibration of the hinged particle-reinforced metamaterial beam under a point force. However, our eq.(4.36) and expression of the midpoint force are of the same form as eqs.(12) & (10) with (11) of [42] or (2) & (14) with (15) of [43]. So, the above derivation for the forced vibration of the hinged metacomposite beam driven by a point force at midway is validated to some extent.

4.4.2 Vibration isolation under a point force at midway

Let us still consider a hinged steel sphere-polyester composite beam, however, driven by a point force at its midway. Likewise, three cases of the excitation frequency are discussed here: (a) below,

(b) within and (c) above the bandgap (as shown in Fig. 4.11).

What is plotted in Fig. 4.11 is the forced vibration of a hinged steel sphere-polyester composite beam driven by a point force at midway based on eqs.(4.36, 4.37). From Fig. 4.11(b), we can find that, for bandgap frequencies, a peak appears at the midpoint where the external force is applied while the forced vibration is vanishingly small in all other parts. In addition, the maximum deflection at the midpoint increases with the excitation frequency within the bandgap, which is further illustrated by Fig. 4.12. However, for excitation frequencies below or above the bandgap shown as Fig. 4.11(a) & (c), the forced vibration always spreads into the entire hinged beam. It is also verified that the wavelength of the forced vibration modes in Fig. 4.11(a) & (c) is much larger than ($2R$), which satisfies the "long-wavelength" condition. Moreover, Fig. 4.13 demonstrates that the amplitude of the forced vibration linearly increases with the magnitude of the applied force under a given excitation frequency.

Like Fig. 4.5 & 4.9, Fig. 4.14 presents the effect of the length of the hinged beam on the forced vibrational mode under an external harmonic force with the excitation frequency within the bandgap. The width of the localized mode around the midpoint in Fig. 4.14 is approximately equal to D for a given harmonic force and excitation frequency within the bandgap. Therefore, the width of the localized mode is independent of the length of the hinged rigid sphere-reinforced metacomposite beam driven by a point force at midway. Also, the width of the localized mode is unaffected by the magnitude of the applied excitation under a given bandgap frequency as shown in Fig. 4.15. Besides, the length of the hinged beam has no impact on the maximum deflection at the midpoint as well.

As a result, a hinged rigid sphere-reinforced metacomposite beam driven by a point force at midway can exhibit the evident vibration isolation behavior and the relevant phenomena appear like those under vibrating ends.

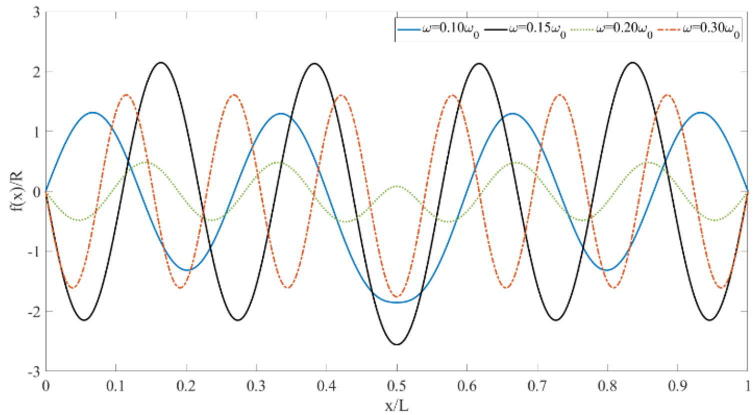

(a)

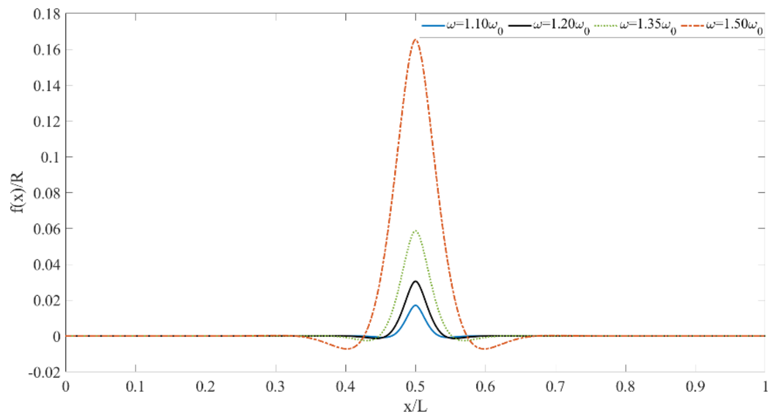

(b)

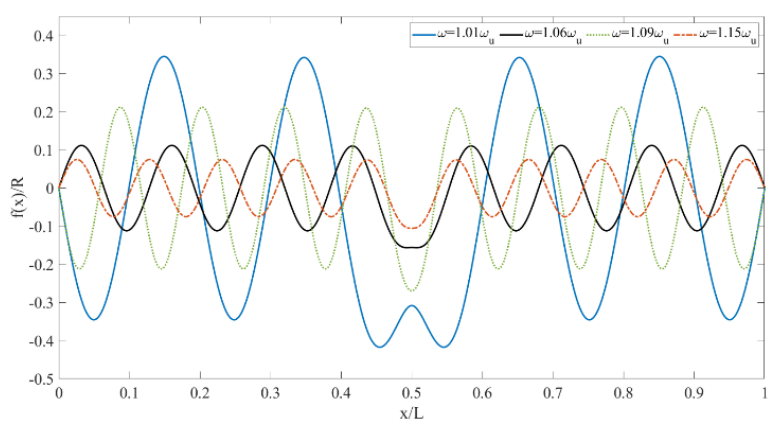

(c)

Fig. 4.11 Forced vibration mode of a hinged steel sphere-polyester composite beam driven by a point force at its midway under different excitation frequencies ω: (a) $\omega < \omega_0$, (b) $\omega_0 < \omega < \omega_u$ and (c) $\omega > \omega_u$, where D=1 cm, L=10D, R=0.5 mm, ρ_s= 7800 kg/m^3, ρ_m= 1220 kg/m^3, $(c_s)_m$=1180 m/s, $(c_l)_m$=2490 m/s, δ=0.184 and Q_0=80 kN

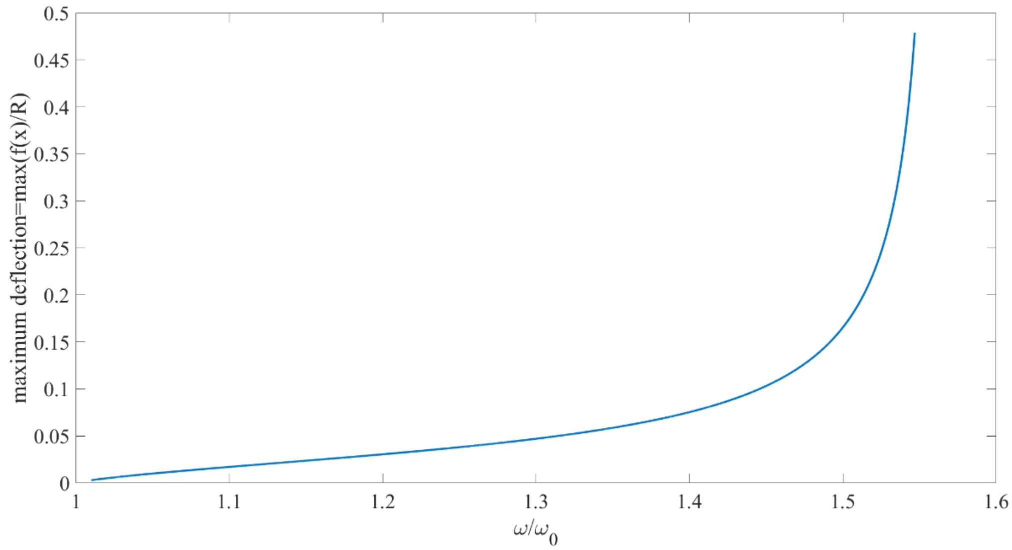

Fig 4.12 Maximum deflection of a hinged steel sphere-polyester composite beam driven by a point force at its midway under different excitation frequencies within the bandgap, where D=1 cm, L=10D, R=0.5 mm, ρ_s= 7800 kg/m^3, ρ_m= 1220 kg/m^3, $(c_s)_m$=1180 m/s, $(c_l)_m$=2490 m/s, δ=0.184 and Q_0=80 kN

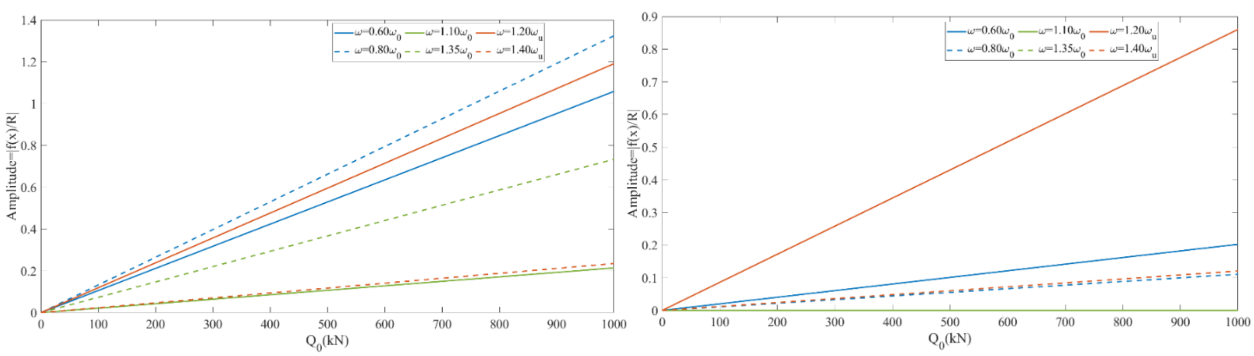

(a) (b)

Fig. 4.13 Amplitude of the forced vibration of a hinged steel sphere-polyester composite beam at (a) x/L=0.5 & (b) x/L=0.8 under different values of the midpoint force Q_0, where D=1 cm, L=10D, R=0.5 mm, ρ_s= 7800 kg/m^3, ρ_m= 1220 kg/m^3, $(c_s)_m$=1180 m/s, $(c_l)_m$=2490 m/s and δ=0.184

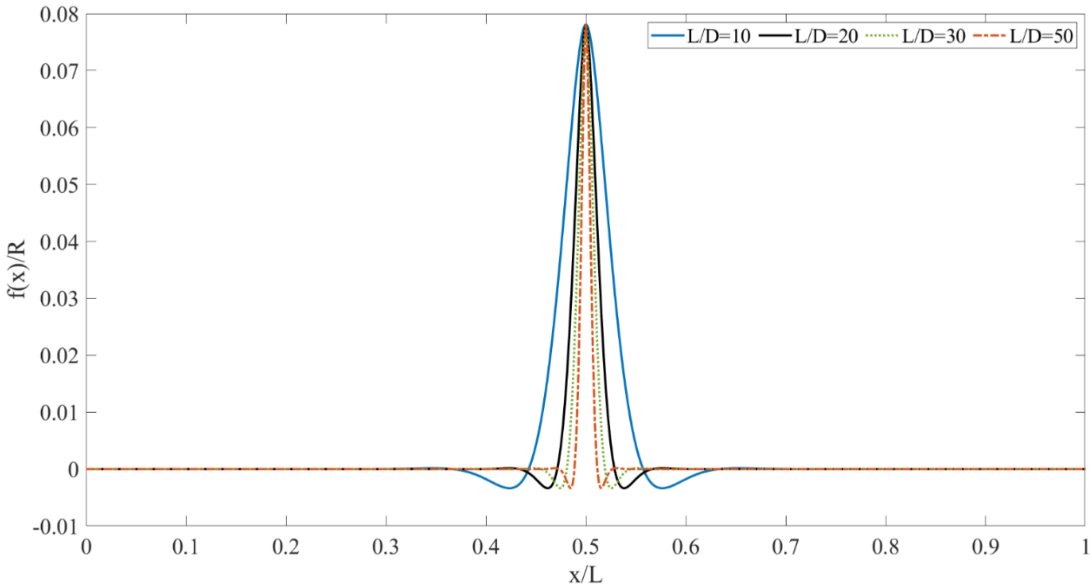

Fig. 4.14 Forced vibrational mode of a hinged steel sphere-polyester composite beam driven by a point force at its midway with different length-to-diameter ratio, where ω=0.90ω_u, D=1 cm, R=0.5 mm, ρ_s= 7800 kg/m^3, ρ_m= 1220 kg/m^3, $(c_s)_m$=1180 m/s, $(c_l)_m$=2490 m/s, δ=0.184 and Q_0=80 kN

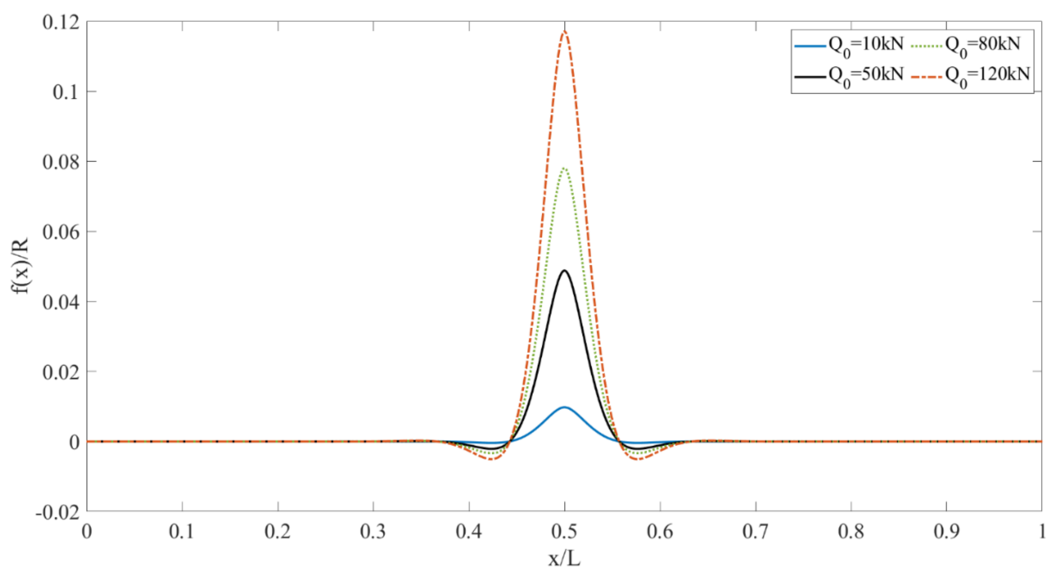

Fig. 4.15 Forced vibrational mode of a hinged steel sphere-polyester composite beam under different values of the midpoint force Q_0, where ω=0.90ω_u, D=1 cm, L=10D, R=0.5 mm, ρ_s= 7800 kg/m^3, ρ_m= 1220 kg/m^3, $(c_s)_m$=1180 m/s, $(c_l)_m$=2490 m/s and δ=0.184

Chapter 5

Vibration of a rigid sphere-reinforced metacomposite rod

To demonstrate the efficiency of the present model, let us apply the model to study axial motion of a rigid sphere-reinforced composite rod [47-50]. On using (2.6) and the 1D form of eq.(2.2)

$$\rho A \frac{\partial^2 u_{mass}}{\partial t^2} = EA \frac{\partial^2 u}{\partial x^2} + F(x,t)\,, \tag{5.1}$$

where A is the cross-sectional area of the rod, and $u_{\mathrm{mass}}(x,t)$ is expressed in terms of $u(x,t)$ as

$$u_{mass} = u + \frac{\rho_s}{\beta}\frac{\rho_m}{\rho}(1-\delta)\frac{\partial^2 u}{\partial t^2} - \frac{\rho_s}{\beta\rho}\left[E\frac{\partial^2 u}{\partial x^2} + \frac{F(x,t)}{A}\right], \tag{5.2}$$

where $F(x,t)$ is the external axial force (per unit axial length) applied to the rod, and $u_{\mathrm{mass}}(x,t)$ is the axial displacement of the mass center of the representative unit cell, while $u(x,t)$ is the axial displacement of the composite rod. Substituting this expression (5.1) to the above eq.(5.2), the equation for $u(x,t)$ is given as follows

$$\rho\left(1 + \frac{\rho_s}{\beta}\frac{\rho_m}{\rho}(1-\delta)\frac{\partial^2}{\partial t^2}\right)\frac{\partial^2 u}{\partial t^2} = E\left(1 + \frac{\rho_s}{\beta}\frac{\partial^2}{\partial t^2}\right)\frac{\partial^2 u}{\partial x^2} + \left(1 + \frac{\rho_s}{\beta}\frac{\partial^2}{\partial t^2}\right)\frac{F}{A}\,. \tag{5.3}$$

Thus, the effective mass density given by (5.3) is of the form

$$\rho_{effective} = \rho_m(1-\delta)\left[1 + \frac{\delta\rho_s}{\rho_m(1-\delta)}\left(\frac{\omega_0^2}{\omega_0^2 - \omega^2}\right)\right], \tag{5.4}$$

which is coincident with (3.4) and becomes negative in the bandgap defined by (3.5).

5.1 Free vibration of a metacomposite rod

For the free vibration of a rigid sphere-reinforced metacomposite rod of length L fixed at x=0 with F=0, $u|_{x=0} = u'|_{x=L} = 0$. Thus, let us consider its axial displacement as

$$u(x,t) = \sin\frac{(2m-1)\pi x}{2L}e^{i\omega t}\,, (m = 1, 2\, \ldots). \tag{5.5}$$

Then, the above eq.(5.3) gives

$$E\left(1-\frac{\rho_s}{\beta}\omega^2\right)\left(\frac{(2m-1)\pi}{2L}\right)^2=\rho\left(1-\frac{\rho_s}{\beta}\frac{\rho_m}{\rho}(1-\delta)\omega^2\right)\omega^2\,. \tag{5.6}$$

Let the two natural frequencies for each mode number m (≥ 1) be (ω_1, ω_2), where $\omega_2 \geq \omega_1$, determined by the following equation of (ω^2)

$$a\omega^4+b\omega^2+c=0\,,\omega_{1,2}^2=\frac{-b\mp\sqrt{b^2-4ac}}{2a}=\left(-\frac{b}{2a}\right)\left(1\mp\sqrt{1-\frac{4ac}{b^2}}\right), \tag{5.7}$$

where

$$a=\frac{\rho_s\rho_m(1-\delta)}{\beta}>0, b=-\left(E\frac{\rho_s}{\beta}\left(\frac{(2m-1)\pi}{2L}\right)^2+\rho\right)<0, c=E\left(\frac{(2m-1)\pi}{2L}\right)^2>0. \tag{5.8}$$

Since $\rho \geq \rho_m(1-\delta)$, it follows that

$$\left(E\frac{\rho_s}{\beta}\left(\frac{(2m-1)\pi}{2L}\right)^2+\rho\right)^2\geq 4\frac{\rho_s\rho_m(1-\delta)}{\beta}\left[E\left(\frac{(2m-1)\pi}{2L}\right)^2\right]. \tag{5.9}$$

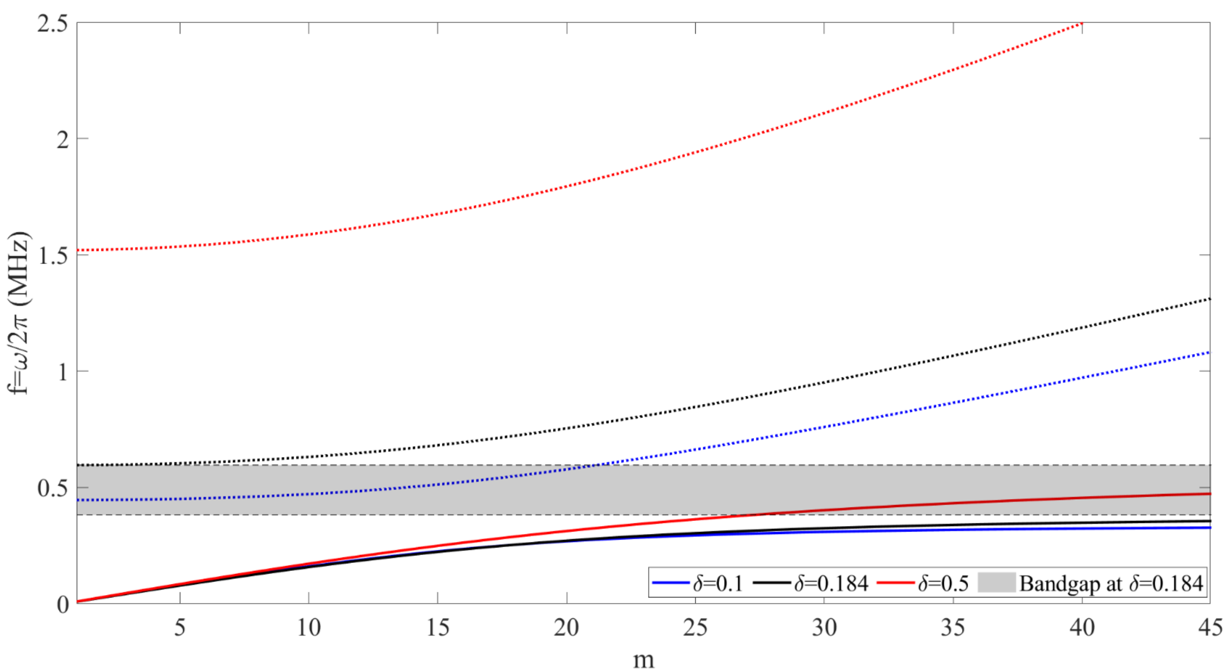

Fig. 5.1 Natural frequencies of a steel sphere-polyester composite rod, as a function of the mode number m for different volume fractions, with the length L=5 cm and the radius of steel spheres R=0.5 mm, where ρ_s= 7800 kg/m^3, ρ_m= 1220 kg/m^3, $(c_s)_m$=1180 m/s and $(c_l)_m$=2490 m/s

So, b^2-4ac≥0 holds through (5.9), and the two roots (ω^2) of (5.7) are strictly positive and bounded by lower and upper cut-off frequencies, ω_0 and ω_u. Fig. 5.1 shows the natural frequencies of a steel-sphere polyester composite rod, which stay outside of the bandgap [ω_0, ω_u] as well. And the bandgap exhibited in Fig. 5.1 is same as that in Fig. 4.1 or 4.2, which is determined by formulas (3.5, 3.6), independent of all other material and geometrical parameters. And ω_0 & ω_u are still consistent with the experimental data of [20] at δ=0.184 and increase with the volume fraction of the rigid spheres.

5.2 Vibration isolation of a metacomposite rod

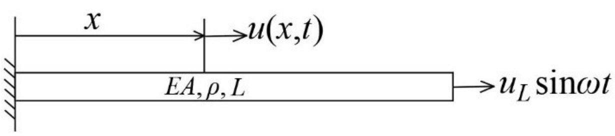

Fig. 5.2 A schematic diagram of a rod with a fixed end and driven by a harmonic axial displacement at its free end

To demonstrate vibration isolation of a stiff sphere-reinforced metacomposite rod, let us examine the forced vibration of the composite rod of length L fixed at x=0 and driven by a harmonic axial displacement at its free end (x=L) with F=0 (see Fig. 5.2). Thus, we have

$$\rho\left(1+\frac{\rho_s}{\beta}\frac{\rho_m}{\rho}(1-\delta)\frac{\partial^2}{\partial t^2}\right)\frac{\partial^2 u}{\partial t^2}=E\left(1+\frac{\rho_s}{\beta}\frac{\partial^2}{\partial t^2}\right)\frac{\partial^2 u}{\partial x^2},$$

$$u|_{x=0}=0\,,u|_{x=L}=u_L\sin\omega t\,. \tag{5.10}$$

where u_L is a constant. In particular, for a classical elastic composite rod (with β=∞), the forced vibration driven by the end displacement is given by

$$u(x,t)=u_0(x)\sin\omega t\,,u_0(x)=u_L\frac{\sin\left[\sqrt{\frac{\rho}{E}}\omega x\right]}{\sin\left[\sqrt{\frac{\rho}{E}}\omega L\right]}, \tag{5.11}$$

whose vibration mode $u_0(x)$ has a harmonically varying amplitude along the entire rod. For a rigid sphere-reinforced metacomposite rod with a finite value of β, however, the solution of (5.10) when ω falls within the bandgap (3.5) is given by

$$u(x,t) = u_0(x)\sin\omega t\,, u_0(x) = u_L \frac{e^{\frac{\lambda x}{L}} - e^{-\frac{\lambda x}{L}}}{e^{\lambda} - e^{-\lambda}};$$

$$\lambda = \omega L \sqrt{\left(\frac{\rho}{E}\frac{\left(\frac{\rho_m \rho_s}{\beta\rho}(1-\delta)\omega^2 - 1\right)}{\left(1 - \frac{\rho_s}{\beta}\omega^2\right)}\right)} > 0. \quad (5.12)$$

It is verified that the amplitude of the vibration mode (5.12) monotonically decays from the free end x=L to the fixed end x=0. In particular, when the excitation frequency ω is within the bandgap and approaches the lower cut-off frequency ω_0, the positive dimensionless parameter λ approaches infinity and the forced vibration mode $u_0(x)$ is extremely localized around the free end x=L but vanishingly small in the entire rod except an infinitesimal neighborhood around the free end.

As an example, the forced vibrational mode of a steel sphere-reinforced polyester rod is shown in Fig. 5.3 with the same cases of the exciting frequency: within and out of the bandgap. It is found from Fig. 5.3(b) that the forced vibrational mode is highly localized near the stimulating end x=L when the exciting frequency ω falls within the bandgap. Otherwise, the forced vibrational mode is a periodic wave through the entire rod when ω is much lower than ω_0 in Fig. 5.3(a) or higher than ω_u shown as Fig. 5.3(c). Here, the wavelength of the forced vibration periodic modes shown in Fig. 5.3(a) & (c) is also much larger than (2R), which justifies the applicability of the present long-wavelength model.

In addition, we still examine the dependence of the width of localized mode on the length of the rigid sphere-reinforced metacomposite rod. It is found from Fig. 5.4 that, for a given excitation frequency within the bandgap, the width of localized mode around the stimulating end is almost constant, about 0.75 cm. Thus, the width of localized mode is independent of the length of the rigid sphere-reinforced metacomposite rod as well.

In brief, the similar vibration isolation phenomenon is also obvious on a rigid sphere-reinforced metacomposite rod driven by a harmonic axial displacement at its free end.

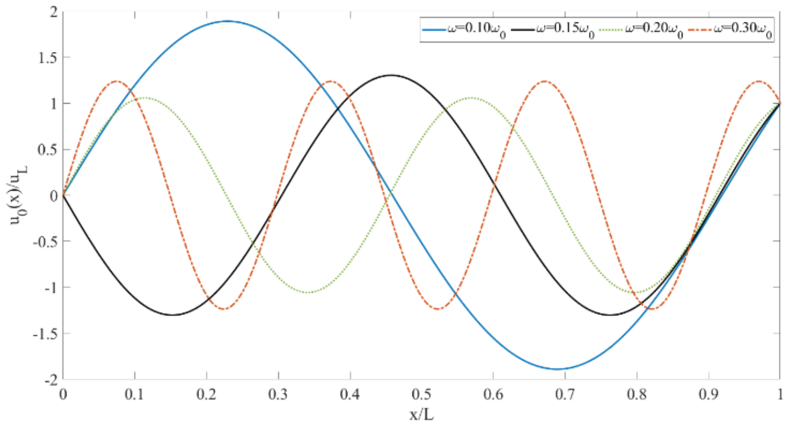

(a)

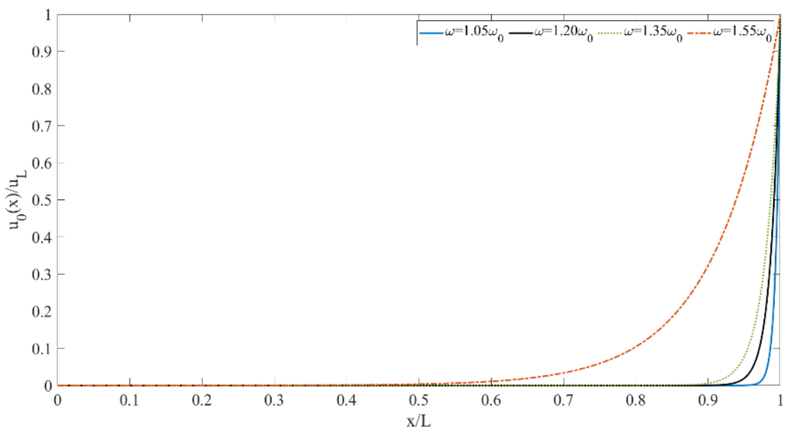

(b)

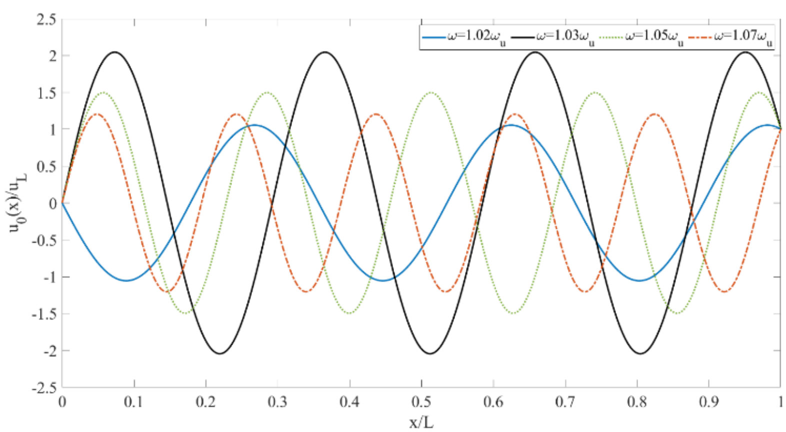

(c)

Fig. 5.3 Forced vibrational mode of a steel sphere-reinforced polyester rod driven by a harmonic axial displacement at the free end x=L (L=5 cm) under different excitation frequencies ω: (a) $\omega < \omega_0$, (b) $\omega_0 < \omega < \omega_u$ and (c) $\omega > \omega_u$, where ρ_s= 7800 kg/m^3, ρ_m= 1220 kg/m^3, $(c_s)_m$=1180 m/s, $(c_l)_m$=2490 m/s, R=0.5 mm and δ=0.184

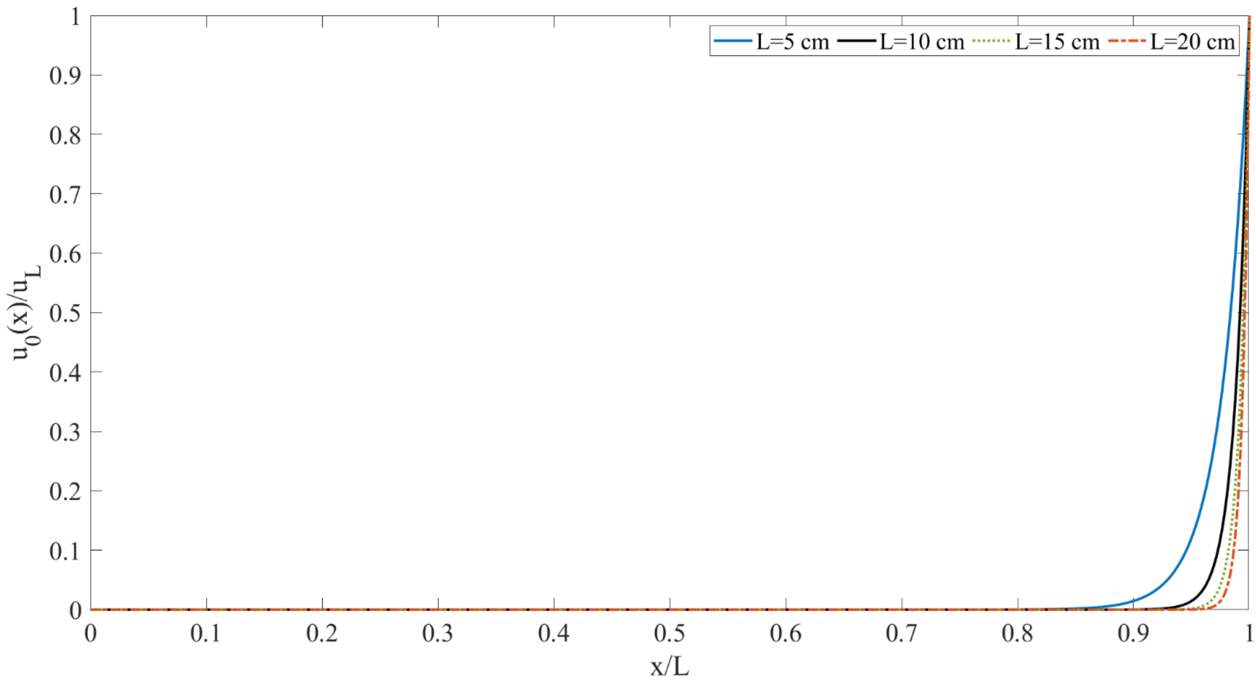

Fig. 5.4 Forced vibrational mode of a steel sphere-reinforced polyester rod driven by a harmonic axial displacement at the free end x=L with different length (L), where ω=0.90ω_u, R=0.5 mm, ρ_s= 7800 kg/m^3, ρ_m= 1220 kg/m^3, $(c_s)_m$=1180 m/s, $(c_l)_m$=2490 m/s and δ=0.184

5.3 Free vibration of a metacomposite rod with an attached mass at its end

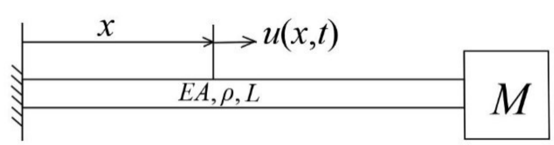

Fig. 5.5 A schematic diagram of a rod with a fixed end and an attached mass at its free end

Now let us examine the effect of an attached mass on the free vibration of a rigid sphere-reinforced metacomposite rod. As shown in Fig. 5.5, the composite rod is fixed at the end x=0 and with a concentrated mass M attached to its other end x=L. Thus, the boundary conditions become

$$u|_{x=0} = 0\,, EA\left.\frac{\partial u}{\partial x}\right|_{x=L} = -M\left.\frac{\partial^2 u}{\partial t^2}\right|_{x=L}\,, \tag{5.13}$$

where M is the attached mass. To study free vibration, substituting $u(x,t)$=$u_0(x)\,sin\omega t$ into (5.13), where ω is the natural frequency, the above boundary conditions are written as

$$u_0|_{x=0} = 0, EA\frac{du_0}{dx}\bigg|_{x=L} = M\omega^2 u_0|_{x=L}\,. \tag{5.14}$$

It follows from (5.3) (with F=0) that $u_0(x) \propto e^{\pm\lambda x/L}$ with the λ-ω relation given by

$$\rho\omega^2 L^2\left(\frac{\rho_S}{\beta\rho}\rho_m(1-\delta)\omega^2 - 1\right) = \lambda^2 E\left(1 - \frac{\rho_S}{\beta}\omega^2\right). \tag{5.15}$$

Let us now show that the natural frequency ω can exist within the bandgap ($\omega_0<\omega<\omega_u$) when such a concentrated mass M>0 is attached to the end $x=L$ of the composite rod. Actually, for the frequency ω within the bandgap ($\omega_0<\omega<\omega_u$), it is seen from (5.15) that λ^2>0. Thus the two roots are $\pm\lambda$ (λ>0), and the end condition (5.14) at $x=L$ gives

$$M\omega^2\frac{(e^{\lambda} - e^{-\lambda})}{(e^{\lambda} + e^{-\lambda})} = \frac{\lambda}{L}EA\,. \tag{5.16}$$

Substituting (5.16) into (5.15), we have the equation for λ>0 as

$$\frac{\left(\lambda\frac{\rho_m(1-\delta)}{\rho}\left(\frac{\chi}{m_0}\right)\frac{(e^{\lambda}+e^{-\lambda})}{(e^{\lambda}-e^{-\lambda})} - 1\right)}{\left(1 - \lambda\left(\frac{\chi}{m_0}\right)\frac{(e^{\lambda}+e^{-\lambda})}{(e^{\lambda}-e^{-\lambda})}\right)} = \lambda m_0\frac{(e^{\lambda}-e^{-\lambda})}{(e^{\lambda}+e^{-\lambda})}\,, \chi = \frac{\rho_S}{\beta}\left(\frac{E}{\rho L^2}\right), m_0 = \frac{M}{\rho AL}\,. \tag{5.17}$$

Clearly, in the absence of the attached mass (M=0), eq.(5.17) has no a positive solution λ>0, which implies the non-existence of natural frequency within the bandgap. For a composite rod with the attached mass M>0, however, the existence of a natural frequency within the bandgap can be confirmed by studying the existence of an intersection of the following function $f(\lambda)$ with the positive horizontal axis

$$f(\lambda) = \frac{\left(\lambda\frac{\rho_m(1-\delta)}{\rho}\left(\frac{\chi}{m_0}\right)\frac{(e^{\lambda}+e^{-\lambda})}{(e^{\lambda}-e^{-\lambda})} - 1\right)}{\left(1 - \lambda\left(\frac{\chi}{m_0}\right)\frac{(e^{\lambda}+e^{-\lambda})}{(e^{\lambda}-e^{-\lambda})}\right)} - \lambda m_0\frac{(e^{\lambda}-e^{-\lambda})}{(e^{\lambda}+e^{-\lambda})}\,. \tag{5.18}$$

Since $f(\lambda)$ given by (5.18) depends on 3 independent parameters: $\rho_m(1\text{-}\delta)/\rho$, χ/m_0 and m_0, our numerical results confirm that, for example, a sufficient condition for the existence of a natural frequency inside the bandgap is $0<\chi/m_0<\rho/[\rho_m(1\text{-}\delta)]$ with $m_0\leq 100$. For example, if we are mainly interested in the physically relevant cases when the attached mass M is comparable to or larger than the rod's mass (ρAL), several cases with m_0=0.01, 0.1, 1, 5 and 100 are shown in Fig. 5.6 (a)-

(f). In particular, it is seen from (2.9) and (5.17) that χ<<1 under the present condition R<<L. For instance, a positive root $\lambda\approx105.3$ exists (which gives $\omega\approx1.026\omega_0$) with m_0=0.1 and χ/m_0=0.01 as shown in Fig. 5.6(a), and a positive root $\lambda\approx100.6$ exists (which gives $\omega\approx1.003\omega_0$) with m_0=1 and χ/m_0=0.01 as shown in Fig. 5.6(c). It is concluded that an attached concentrated mass M can change the total effective mass of the composite rod and gives rise of a natural frequency inside the bandgap defined by (3.5, 3.6).

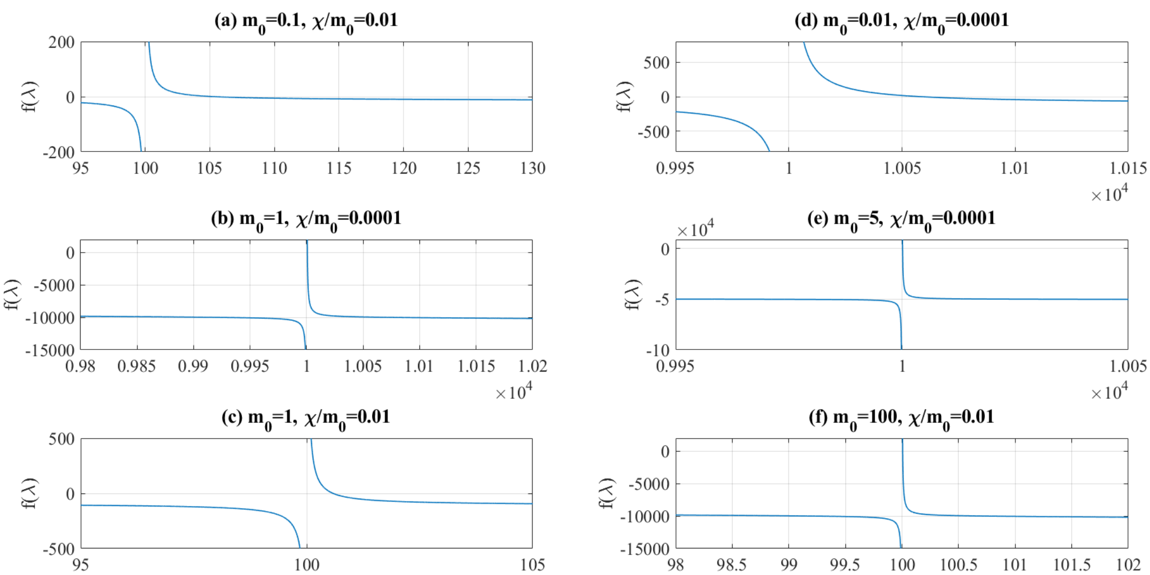

Fig. 5.6 Plots of the function $f(\lambda)$ defined by eq.(5.18) at different values of m_0 and χ/m_0 with the parameters of steel sphere-reinforced polyester, ρ_s= 7800 kg/m^3, ρ_m= 1220 kg/m^3 and δ=0.184

Next, let us examine the free vibration with the natural frequency ω outside the bandgap ($\omega<\omega_0$ or $\omega>\omega_u$). In this case, it follows from (5.15) that $\lambda^2<0$, then the two roots are two opposite pure imaginary numbers, $\lambda=\pm i\alpha$ with $\alpha>0$. With the end x=0 fixed, we have

$$u_0(x) = C\, sin\, \alpha \frac{x}{L}\, , 0 \leq x \leq L\, . \tag{5.19}$$

The end condition (5.14) at x=L gives the α-ω relation

$$\tan\alpha = \frac{EA\alpha}{\omega^2 ML} = \left(\frac{\omega_0}{\omega}\right)^2 \frac{\chi}{m_0}\alpha\, . \tag{5.20}$$

For a given value of α>0, the four roots of ω are two pairs of opposite pure imaginary numbers, ($\pm i\omega_1$) and ($\pm i\omega_2$), respectively, with $\omega_2>\omega_1>0$, where ω_2 and ω_1 are given in terms of α as

$$\left(\frac{\omega_1}{\omega_0}\right)^2 = \frac{(\alpha^2\chi + 1) - \sqrt{(\alpha^2\chi + 1)^2 - 4\alpha^2\chi\frac{\rho_m(1-\delta)}{\rho}}}{2\frac{\rho_m(1-\delta)}{\rho}} < 1\,, \tag{5.21}$$

$$\left(\frac{\omega_2}{\omega_u}\right)^2 = \frac{(\alpha^2\chi + 1) + \sqrt{(\alpha^2\chi + 1)^2 - 4\alpha^2\chi\frac{\rho_m(1-\delta)}{\rho}}}{2} > 1\,. \tag{5.22}$$

Because $\rho>\rho_m(1\text{-}\delta)$, it is readily seen that $\omega_2>\omega_u$. Furthermore, in view of

$$(\alpha^2\chi + 1)^2 - 4\alpha^2\chi\frac{\rho_m(1-\delta)}{\rho} > \left(\alpha^2\chi + 1 - 2\frac{\rho_m(1-\delta)}{\rho}\right)^2\,, \tag{5.23}$$

it is verified that $\omega_1<\omega_0$. Thus, substituting the above expression (5.22) (or (5.21)) of ω_2 (or ω_1) into eq.(5.20), one can determine the discrete values of α and the corresponding values of ω_2 (or ω_1), as shown in Fig. 5.7 for a specific example of steel sphere-reinforced polyester composite rod. It is seen from Fig. 5.7 that the value of α (which determines the wave number of free vibrational mode) increases with ω for both cases $\omega_1<\omega_0$ and $\omega_2>\omega_u$.

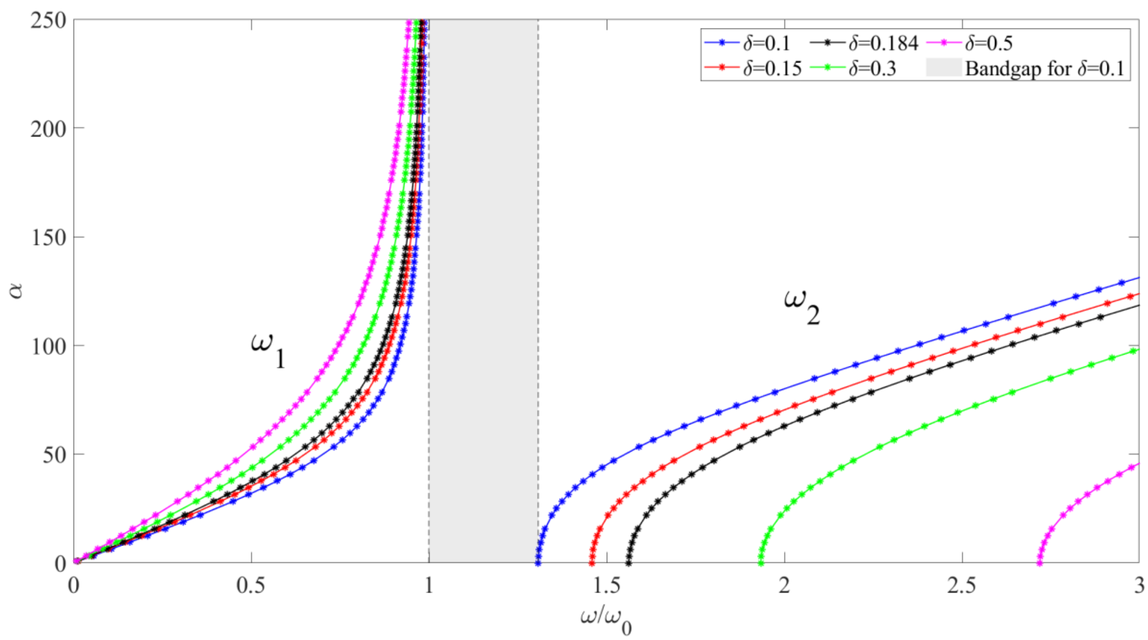

Fig. 5.7 The α-ω_2 (or ω_1) relation for free vibration of a steel sphere-reinforced polyester rod fixed at the end x=0 and with a mass attached to the other end x=L, where ρ_s= 7800 kg/m^3, ρ_m= 1220 kg/m^3, R=0.5 mm, L=5 cm and m_0=1

Chapter 6

Conclusions and future work

6.1 Conclusions

A general analytical model is proposed for dynamics of rigid sphere-reinforced random metacomposites based on the concept that the deviation of the displacement field of embedded rigid spheres from the displacement field of the composite is responsible for dynamic behaviors of the composite. The model is characterized by the well-known elastodynamic equations combined with a simple differential relation between the displacement field of the mass center of representative unit cell and the displacement field of the composite. The efficiency and accuracy of the proposed model are verified by reasonable agreement between the predicted results and known experimental or numerical data on several typical stiff sphere-reinforced polymer composites reported in literature. The proposed model is applied to study several basic dynamic problems of rigid sphere-reinforced composite beams and rods, and the relevant dynamic phenomena (such as vibration isolation, localized buckling, and the natural frequency within the bandgap caused by an attached concentrated mass) are demonstrated.

The major conclusions are summarized below:

(1) Natural frequencies of the rigid sphere-reinforced metacomposite beam or rod always stay outside of the bandgap, independent of all other material and geometrical parameters, consistent with the physical concept of the “bandgap”.

(2) A hinged rigid sphere-reinforced metacomposite beam under a constant compressive load can exhibit localized buckling at the critical buckling state when the mass ratio of the rigid-sphere phase to the matrix phase is vanishingly small.

(3) A rigid sphere-reinforced metacomposite beam or rod can exhibit vibration isolation phenomena. Actually, when the excitation frequency falls within the bandgap, the forced vibration mode is highly localized near the site of the applied external harmonic excitation and vanishing small in all other parts of the beam or rod. The width of localized mode around the site of the applied excitation is independent of the length of the beam or rod and the magnitude of the applied excitation. In contrast to this, when the excitation frequency is out of the bandgap, the forced

vibration mode is a periodic wave through the entire beam or rod. Besides, for a hinged composite beam driven by a midpoint force, the maximum deflection increases with the excitation frequency within the bandgap but is also independent of the length of the beam.

(4) An attached concentrated mass M at the free end can change the total effective mass of the composite rod and gives rise of a natural frequency inside the bandgap.

In summation, it is believed that the present model enjoys the conceptual and mathematical simplicity and could offer a general simple model to study dynamics of rigid sphere-reinforced random metacomposites.

6.2 Future work

In this thesis, we develop a much simple (although approximate) model for general 3D dynamics of stiff sphere-reinforced random metacomposites. As to a future work, we may consider

1). How to make our current model more accurate to evaluate forced vibration of one- or two-dimensional composite structures. For example, we can use more accurate formulas for effective elastic moduli of particle-reinforced elastic composites with higher volume fraction of particles, beyond the simple refined Einstein formulas. In addition, we can consider forced vibration of stiff sphere-reinforced metacomposite plates.

2). Another important future topic is to apply our analytical model to adjusting the design of materials or structures to achieve our desired purpose. For instance, as seen in our Table 3.1, the bandgap frequencies for the glass sphere-reinforced polyester composite almost reach the magnitude of MHz. To lower the bandgap to, say, KHz range, we may attempt to adopt heavier spheres and/or softer matrix, and/or properly reduce the volume fraction of embedded rigid spheres in the design of metamaterials according to our formulas (3.5, 3.6).

Bibliography

[1] V.G. Veselago (1968). The electrodynamics of substances with simultaneously negative values of ε and μ. *Soviet Physics Uspekhi* 10, p509.

[2] Hongwei Sun, Xingwen Du, P.Frank Pai (2010). Theory of Metamaterial Beams for Broadband Vibration Absorption. *Journal of Intelligent Material Systems and Structures* 21, No. 11, pp.1085-1101.

[3] P.Frank Pai, Hao Peng, Shuyi Jiang (2014). Acoustic metamaterial beams based on multi-frequency vibration absorbers. *International Journal of Mechanical Sciences* 79, pp.195–205.

[4] S.H. Lee & O.B. Wright (2016). Origin of negative density and modulus in acoustic metamaterials. *Phys. Rev. B.* 93, 024302.

[5] Zhengyou Liu, Xixiang Zhang, Yiwei Mao, Y.Y. Zhu, Zhiyu Yang, C.T. Chan, Ping Sheng (2000). Locally Resonant Sonic Materials. *Science* 289, p1734.

[6] M.M. Sigalas, M.S. Kushwaha, E.N. Economou, M. Kafesaki, I.E. Psarobas, W. Steurer (2005). Classical vibration modes in phononic lattices: theory and experiment. *Z. Kristallogr.* 220, pp.765-809.

[7] Emilio P. Calius, Xavier Bremaud, Bryan Smith, Andrew Hall (2009). Negative mass sound shielding structures: Early results. *Phys. Status Solidi B* 246, No. 9, p2089.

[8] Kathryn H. Matlack, Anton Bauhofer, Sebastian Krödel, Antonio Palermo, Chiara Daraio (2016). Composite 3D-printed metastructures for low-frequency and broadband vibration absorption. *Proceedings of the National Academy of Sciences* 113, No. 30, pp.8386-8390.

[9] X. Xiao, Z.C. He, Eric Li, A.G. Cheng (2019). Design multi-stopband laminate acoustic metamaterials for structural-acoustic coupled system. *Mechanical Systems and Signal Processing* 115, No. 15, pp.418-433.

[10] R. Zhu, X.N. Liu, G.K. Hu, C.T. Sun, G.L. Huang (2014). A chiral elastic metamaterial beam for broadband vibration suppression. *Journal of Sound and Vibration* 333, No. 10, pp.2759-2773.

[11] Antonio Schiavone & Xiaodong Wang (2022). Continuous modelling of a class of periodic elastic metamaterials with local rotation. *Z. Angew. Math. Phys.* 73, 29.

[12] F.C. Moon & C.C. Mow (1970). Wave propagation in a composite material containing dispersed rigid spherical inclusions. RM-6139-PR. Rand Santa Monica, California (USA).

[13] V.K. Kinra, E. Ker, S.K. Datta (1982). Influence of particle resonance on wave propagation

in a random particulate composite. *Mechanics Research Communications* 9, No. 2, pp.109-114.
[14] V.K. Kinra & P. Li (1986). Resonant scattering of elastic waves by a random distribution of inclusions. *International Journal of Solids and Structures* 22, No. 1, pp.1-11.
[15] F. C. Wong & A. Ait Kadi (1995). On the Prediction of Mechanical Behavior of Particulate Composites Using an Improved Modulus Degradation Model. *Journal of Composite Materials* 31, No. 2, pp.104-127.
[16] M. Kafesaki, M.M. Sigalas, E.N. Economou (1995). Elastic wave band gaps in 3-D periodic polymer matrix composites. *Solid State Communication* 96, No. 5, p285.
[17] V.K. Kinra, N.A. Day, K. Maslov, B.K. Henderson, G. Diderich (1998). The transmission of a longitudinal wave through a layer of spherical inclusions with a random or periodic arrangement. *J. Mech. Phys. Solids* 46, No. 1, p153.
[18] K. Maslov & V.K. Kinra (1999). Acoustic response of a periodic layer of nearly rigid spherical inclusions in an elastic solid. *Journal of the Acoustical Society of America* 106, p3081.
[19] K. Maslov, V.K. Kinra, B.K. Henderson (2000). Elastodynamic response of a coplanar periodic layer of elastic spherical inclsuions. *Mechanics of Materials* 32, pp.785-795.
[20] R. Sainidou, N. Stefanou, A. Modinos (2002). Formation of absolute frequency gaps in three-dimensional solid phononic crystals. *Physical Review B* 66, 212301.
[21] J. Cheng, Z.L. Liu, C.C. Luo, T. Li, Z.J. Li, Y. Kang, Z. Zhuang (2020). Revealing the high-frequency attenuation mechanism of polyurea-matrix composites. *Acta Mechanica Sinica* 36, No. 1, pp.130–142.
[22] Mohammad Rahimzadeh (2022). Analysis of the Effective Dynamic Properties of Particulate Composites with Respect to Constituent Properties. *Latin American Journal of Solids and Structures* 19, No. 2, p429.
[23] J. Segurado & J. Llorca (2002). A numerical approximation to the elastic properties of sphere-reinforced composites. *J. Mech. Phys. Solids* 50, p2107.
[24] S. Kari, H. Berger, R. Rodríguez-Ramos, U. Gabbert (2007). Computational evaluation of effective material properties of composites reinforced by randomly distributed spherical particles. *Composite Structures* 77, pp.223–231.
[25] G. Bourkas, I. Prassianakis, V. Kytopoulos, E. Sideridis, C. Younis (2010). Estimation of elastic moduli of particulate composites by new models and comparison with moduli measured by tension, dynamic, and ultrasonic tests. *Advances in Materials Science and Engineering*, 891824.

[26] Yunhua Luo (2021). Isotropized Voigt-Reuss model for prediction of elastic properties of particulate composites. *Mechanics of Advanced Materials and Structures*, 1913772.

[27] Yunhua Luo (2022). Microstructure-free finite element modeling for elasticity characterization and design of fine-particulate composites. *J. Compos. Sci.* 6, No. 2, p35.

[28] Darius Zabulionis & Vytautas Rimša (2018). A lattice model for elastic particulate composites. *Materials* 11, No. 9, p1584.

[29] G.W. Milton & J.R. Willis (2007) On modifications of Newton's second law and linear continuum elastodynamics. *Proc. R. Soc.A* 463, p855.

[30] Selvadurai APS. (2016) Indentation of a spherical cavity in an elastic body by a rigid spherical inclusion. *Continuum Mech. & Thermodynamics* 28, p617.

[31] M. Puljiz & A.M. Menzel (2017) Forces and torques on rigid inclusions in an elastic environment. *Phy. Rev.E* 95, 053002.

[32] H.S. Chen & A. Acrivos (1978). The effective elastic moduli of composite materials containing spherical inclusions at non-dilute concentrations. *International Journal of Solids and Structures* 14, No. 5, p349.

[33] R.M. Christensen (2004). Effective properties of single size, rigid spherical inclusions in an elastic matrix. *Composites: part B* 35, p475.

[34] S.Y. Fu, X.Q. Feng, B. Lauke, Y.W. Mai (2008). Effects of particle size, particle/ matrix interface adhesion and particle loading on mechanical properties of particulate-polymer composites. *Composites: Part B* 39, p933.

[35] A. Banerjee (2020) Non-dimensional analysis of the elastic beam having periodic linear spring mass resonators. *Mechanica* 55, p1181.

[36] D. Zhou & T. Ji (2006) Dynamic characteristics of a beam and distributed spring-mass system. *International Journal of Solids and Structures* 43, p5555.

[37] Yiwei Xia, Massimo Ruzzene, Alper Erturk (2020). Bistable attachments for wideband nonlinear vibration attenuation in a metamaterial beam. *Nonlinear Dynamics* 102, p1287.

[38] C.E. Repetto, A. Roatta, R.J. Welti (2012). Forced vibrations of a cantilever beam. *European Journal of Physics* 33, p1190.

[39] Mateusz Romaszko, Bogdan Sapiński, Andrzej Sioma (2015). Forced vibrations analysis of a cantilever beam using the vision method. *Journal of Theoretical and Applied Mechanics* 53, p247.

[40] C.G. Johnson, U. Jain, A.L. Hazel, D. Pihler-Puzovic, T. Mullin (2017). On the buckling of an elastic holey column. *Proc. R. Soc.A* 473, 20170477.

[41] V.A. Eremeyev & E. Turco (2019). Enriched buckling for beam-lattice metamaterials. *Mechanics Research Communications* 103, UNSP 103458.

[42] L. Lu, C.Q. Ru & X.M. Guo (2017). Negative effective mass of a filled carbon nanotube. *International Journal of Mechanical Sciences* 134, p176.

[43] L. Lu, C.Q. Ru & X.M. Guo (2020). Vibration isolation of few-layer graphene sheets. *International Journal of Solids and Structures* 185, pp.78-83.

[44] O. Casablanca, G. Ventura, F. Garescì, B. Azzerboni, B. Chiaia, M. Chiappini, G. Finocchio (2018). Seismic isolation of buildings using composite foundations based on metamaterials. *J. Appl. Phys.*123, 174903.

[45] L.G. Bennetts, M.A. Peter, P. Dylejko, A. Skvortsov (2019). Effective properties of acoustic metamaterial chains with low-frequency bandgaps controlled by the geometry of lightweight mass-link attachments. *J. Sound & Vibration* 456, p1.

[46] Di Mu, Haisheng Shu, Shuowei An, Lei Zhao (2020). Free and steady forced vibration characteristics of elastic metamaterial beam. *AIP Advances* 10, 035304.

[47] Jeongwon Park, Buhm Park, Deokman Kim, Junhong Park (2012). Determination of effective mass density and modulus for resonant metamaterials. *J. Acoustic. Soc. Am.* 132, p2793.

[48] K.T. Tan, H.H. Huang, C.T. Sun (2014). Blast-wave impact mitigation using negative effective mass density concept of elastic metamaterials. *Int. J. Impact Engng.* 64, p20.

[49] E.D. Nobrega, F. Gautier, A. Pelat, J.M.C. Dos Santos (2016). Vibration band gaps for elastic metamaterial rods using wave finite element method. *Mechanical Systems & Signal Processing* 79, p192.

[50] A. Ogasawara, K. Fujita, M. Tomoda, O. Matsuda, O.B. Wright (2020). Wave-cancelling acoustic metarod architected by with single material building blocks. *Appl. Phys. Let.* 116, 241904.

END.